Stony Brook University

Defect Analysis of Boron Phosphide Thin Films and Sapphire Single Crystal Using Synchrotron X-ray Topography

A Thesis Presented

by

Zihao Ding

to

The Graduate School

in Partial Fulfillment of the

Requirements

For the Degree of

Master of Science

in

Materials Science and Engineering

Stony Brook University

May, 2014

Stony Brook University

The Graduate School

Zihao Ding

We, the thesis committee for the above candidate for the
Master of Science degree, hereby recommend
acceptance of this thesis.

Michael Dudley – Thesis Advisor
Professor, Department of Materials Science and Engineering

Balaji Raghothamachar– Second Reader
Research Professor, Department of Materials Science and Engineering

T. A. Venkatesh– Third Reader
Associate Professor, Department of Materials Science and Engineering

This thesis is accepted by the Graduate School

Charles Taber
Interim Dean of the Graduate School

Abstract of the Thesis

Defect Analysis of Boron Phosphide Thin Films and Sapphire Single Crystal Using Synchrotron X-ray Topography

by

Zihao Ding

Master of Science

in

Materials Science and Engineering

Stony Brook University

2014

Boron phosphide is an ideal semiconductor material used for neutron detectors because of its superior material properties, such as wide band gap and large thermal neutron capture cross-section of ^{10}B. Since bulk BP is not readily available for neutron detector application, BP thin films are mainly synthesized by chemical vapor deposition (CVD). Among all the feasible substrates for BP deposition, SiC stands out due to its small lattice mismatch (4.5%) with BP, however it is necessary to optimize the growth condition to synthesize high quality BP thin films on SiC. In chapter III, BP thin film samples deposited on 4H-SiC and 6H-SiC under different growth conditions are characterized, mainly using synchrotron X-ray topography and other techniques such as optical microscopy and scanning electron microscopy. The relationship between BP thin film crystal quality and substrate material and orientation and other growth conditions is investigated. It can be concluded from the experimental data that the crystal quality of BP thin films on 4H-SiC substrate is much better than that on 6H-SiC substrate. Besides, poor crystalline quality of substrate will likely degrade the crystalline quality of epitaxial thin films.

Sapphire single crystal has been widely used in high-technology industry because of its excellent combination between optical, electrical and mechanical properties. In this thesis, a-plane sapphire ribbon grown by Edge-defined Film-fed Growth method (EFG) is

analyzed by characterizing the seed crystals used and the quality of as-grown ribbon, by reflection X-ray topography. Distributions and formation mechanisms of defects inside both the sapphire seed crystal and ribbon crystal are studied. Transmission topographs reveal the presence of two sets of slip bands that are nucleated from either edge, the distribution of which is symmetric in the used seed crystal and asymmetric in the pristine seed crystal. This phenomenon could be caused by the unstable growth condition. As in sapphire ribbon, reflection topographs reveal features that indicate interface instability and asymmetric columnar crystal growth near the ribbon shoulder, which eventually lead to polycrystallinity at bottom of the sapphire ribbon.

TABLE OF CONTENTS

LIST OF FIGURES AND TABLES

LIST OF ABBREVIATIONS

XRT	X-ray Topography
SWBXT	Synchrotron White Beam X-ray Topography
CVD	Chemical Vapor Deposition
EFG	Edge-defined Film-fed Growth
SEM	Scanning Electron Microscopy
BPD	Basal Plane Dislocation
LAGB	Low Angle Grain Boundary

ACKNOWLEDGMENTS

First of all I would like to present my deep and sincere gratitude to my advisor, Professor Michael Dudley, for offering me this valuable opportunity to study in the field of defect analysis by synchrotron X-ray topography. His wide knowledge and helpful guidance have been of great value for me. Undoubtedly his understanding, encouragement and guidance have always been an inspiration for my research.

I would like to thank Dr. Balaji Raghothamachar for his helpful guidance during experiments and valuable suggestion and discussion during the entire research project.

I would like to thank Professor T. A. Venkatesh for being in my committee member and his help and suggestion during my research project.

I would like to present my true gratitude to my girlfriend Miss. Ruifen Chen for her meticulous care and company during this period, which would be an unforgettable memory in my life.

I would also like to thank my colleagues: Mr. Fangzhen Wu, Ms. Huanhuan Wang, Mr. Shayan Byrappa, Ms. Hao Wang, Ms. Shun Sun, Mr. Goue Ouloide Yannick, Ms. Yu Yang, Mr. Jianqiu Guo and Mr. Zheyu Li for their help and during my research.

Finally, I would like to thank my parents Mr. Liming Ding and Mrs. Jianying Lu, for their great assistance during my study. Without them, I could not efficiently complete my thesis and acquire knowledge.

Chapter I. INTRODUCTION

1.1 Introduction of Boron Phosphide Thin Films

Boron phosphide is a promising candidate material for highly efficient solid-state neutron detectors, due to its wide band gap and large thermal neutron capture cross-section of ^{10}B, also it possesses high thermoelectric power at high temperature, which makes it superior to Si or other III-V semiconductor materials for thermoelectric devices[1][2].

Boron has two forms of phosphides: (1) cubic monophosphide (BP) with a band gap of 2.0 eV and (2) Rhombohedral subphosphide ($B_{12}P_2$) with a band gap of 3.3 eV[3][4]. Fig 1-1 shows structures of BP and $B_{12}P_2$ respectively. In the cubic BP unit cell, boron atoms occupy half of the tetrahedral sites in the face-centered cubic unit cell that constructed by phosphorous atoms, while in $B_{12}P_2$, two phosphorous atoms sit inside the rhombohedral frame that composed by eight B_{12} icosahedra. Monophosphide (BP) can decompose into $B_{12}P_2$ at high temperature (1100°C)[5].

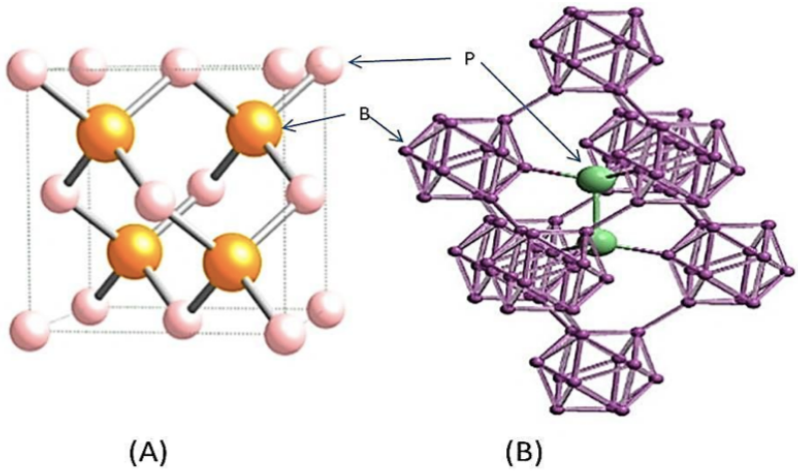

Fig. 1-1 Atomic structures of (A) Cubic monophosphide (BP); (B) Rhombohedral subphosphide ($B_{12}P_2$).

The method to synthesis BP thin film in this thesis is chemical vapor deposition (CVD), using 4H-SiC and 6H-SiC as the substrate material due to the acceptably small mismatch (4%) between the epitaxial layer and the substrate. The stacking relation between the BP layer and SiC substrate is normally described as: (0001)-SiC//(111)-BP, since the minimum lattice mismatch strain is generated when (0004)-SiC (with a d-spacing d_{0004}=0.251 nm for 4H-SiC) and (111)-BP (d_{111}=0.262 nm) are matched.

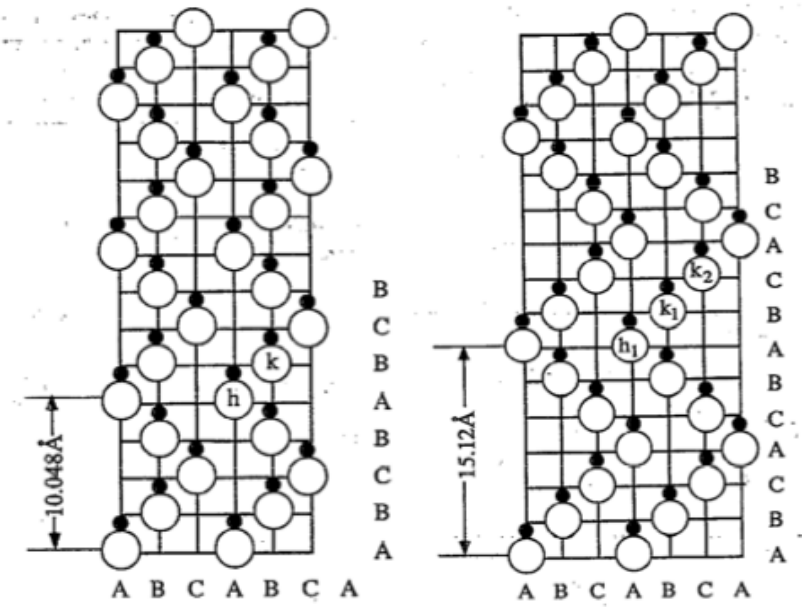

Fig.1-2 Atomic models of 4H-SiC (Left) and 6H-SiC (Right)[6].

Atomic models of 4H-SiC and 6H-SiC are shown in Fig. 1-2, which are the most commonly used polytypes of SiC as substrates for BP. Different polymorphs of SiC has a different stacking sequence of atomic layers, as labeled as A, B, and C. The numbers in 4H-SiC and 6H-SiC stand for the number of layer in one unit cell and the letter indicates the Bravais lattice, H for hexagonal. As shown above, 4H-SiC possesses a stacking sequence of "BCBA" while 6H-SiC has a "BCACBA" stacking of atomic planes. The lattice constant along c-axis is therefore different in the two polymorphs, as labeled in the figure. 3C-SiC has relatively fewer commercial applications because it's difficult to synthesize high quality single crystal 3C-SiC substrate for epitaxial layer growth. As a matter of fact, all commercialized SiC wafers have been cut and polished 3° to 8° off the (0001) basal plane, which, as expected, facilitates the deposition process of BP[7,8].

However, crystal twinning remains as the most common problem during the BP deposition on SiC substrate, since cubic BP has a three-fold symmetry along [111] direction and thus resulting in two oriented BP crystals when deposited on the six-fold-symmetric SiC hexagonal lattice along c-axis. The two possible BP crystals could nucleate on the (0001) basal plane with equal chance. Fig. 1-3 shows the optical microscope image of different oriented BP crystallites from isolated triangular crystals to the as-grown BP thin film with 60° and 120° features.

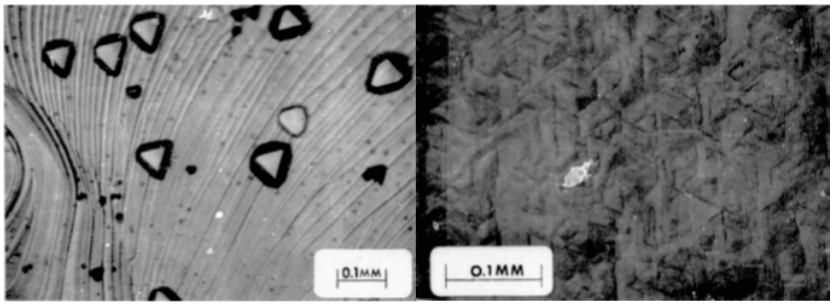

Fig.1-3 Optical microscope image of two oriented BP crystallites deposited on SiC substrate[9].

1.2 Introduction of Sapphire Single Crystal

Sapphire single crystals (α-Al_2O_3) are widely used in high technology industry, because of its excellent combination between optical and mechanical properties. As an application for precision mechanical parts, single crystal sapphire exerts high strength, excellent anti-abrasion, anti-heat and anti-corrosion characteristics[10]. Besides these advantages, single crystal sapphire also possesses a stable dielectric constant, good electrical insulation as well as a wide transmission wavelength range, which in total make it an exceptional material for optical windows, substrates and construction units[20,21]. Physical, thermal and electrical characteristics of single crystal sapphire are listed in the table below.

Tab. 1-1 Physical, thermal and electrical properties of single crystal sapphire[11].

Physical Characteristics		**Thermal Characteristics**	
Structure	Hexagonal-rhombohedral	Melting Point (°C)	2050
Lattice constants (Å)	a=4.675; c=13.000	Thermal conductivity (W/mK) at 20°C	41.9
Crystal density (g/cm^3)	3.98	Thermal Expansion (20-1000°C)	Parallel to C-axis: 9.03×10^{-6}°C
Hardness	9 Mohs	**Electrical Characteristics**	
Young Modulus (GPa)	379 at 30° to C-axis	Dielectric Constant	11.5 parallel to C-axis
Tensile strength	400 at 25°C	Dielectric strength (V/cm)	4×10^5

The single crystal sapphire unit cell is a hexagonal structure, as shown in Fig. 1-4(a) and (0001) plane view shown in Fig. 1-4(b). Sapphire belongs to $D_{3d}^{6} - R\bar{3}C$ space group[12] and it has the same symmetry with wurtzite GaN, making it the well-matched and most economical substrate to construct a GaN based LED device.

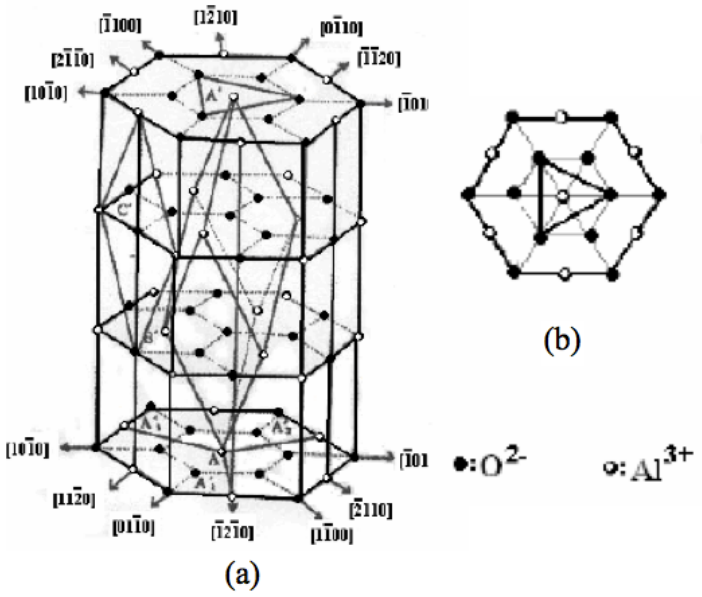

Fig. 1-4 The structure of single crystal sapphire: (a) Unit cell structure; (b) (0001) surface structure.

1.3 Fundamentals of Synchrotron X-ray Diffraction Topography

X-ray diffraction has been widely used by mineralogists, chemists and material scientists to study structures of a variety of materials. X-ray is a type of electromagnetic radiation with a much shorter wavelength than visible light (0.5-2.5Å)[13]. The properties of electromagnetic wave make X-ray a unique technique in modern science. When incident X-ray interacts with planes of atoms in the crystal, it can result in a constructive interference (which means scattered waves reinforce each other) if Bragg's equation is satisfied.

$$\lambda = 2d \sin\theta$$

Where λ is the wavelength of the incident X-ray beam, d is the interplaner spacing of the diffracting atomic plane, and θ is angle between the incident ray and the atomic plane.

In order to understand X-ray diffraction phenomena in crystalline materials, kinematic and dynamical theories of X-ray are employed[14]. Laue's kinematical theory is useful for small imperfect crystals, however the diffracted intensity thus predicted to continuously increase with

the increasing size of a crystal, which apparently contradicts the conservation of energy. Dynamical theory is then employed because it takes into account the whole wave field inside a crystal while diffraction occurs as an entity.

X-ray topography is a nondestructive imaging technique to investigate defects in nearly perfect single crystalline materials, by means of X-ray diffraction[15]. In this technique, a low-divergence area-filling X-ray beam illuminates a single crystal. Diffracted X-rays from atomic planes set at the right Bragg angles is projected onto a two-dimensional detector (usually photographic film, CCD detector or a nuclear plate).

Synchrotron radiation is an extraordinary scientific instrument that is exploited for a variety of fields of research on materials' structures and properties. Because of its advantages in high brightness and low divergence of the X-ray beam, synchrotron radiation is especially suitable for X-ray topography and extremely high resolution can be achieved[16]. The topographic resolution (R) is determined by the source size of the incident beam (S), source-specimen distance (D) and the specimen-film distance (d), as in the equation[17]:

$$R = dS/D.$$

A white beam X-ray is a polychromatic X-ray beam that contains X-ray energies from about 6 keV to 50 keV with an X-ray wavelength from 0.25 Å to 2 Å[15]. When a white beam X-ray is used for topography, images that come from different atomic planes are acquired simultaneously as each set of plane chooses its satisfied wavelength and energy of the X-ray at a specific angle. In Fig. 1-5, where a schematic of SWBXT method is demonstrated, each X-ray diffraction spot on the film represents for a set of atomic planes that satisfy Bragg's equation.

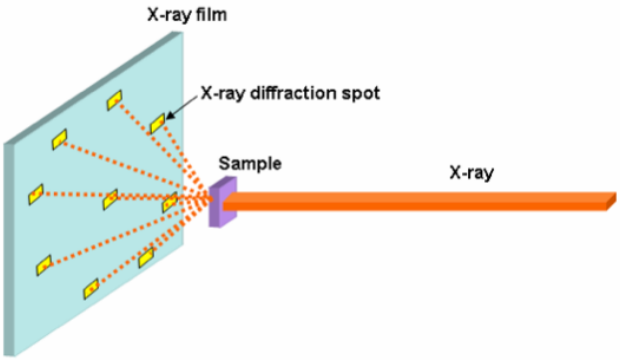

Fig. 1-5 Schematic of SWBXT method. (Transmission geometry)

By the technique of synchrotron white beam X-ray topography (SWBXT), most defects in

single crystal, such as dislocations, stacking fault, small angle grain boundary, inclusion and surface damage, can be observed and recorded in the form of a topograph. Topographic contrast arises from differences in the diffracting power that is a result of complex interactions between X-ray and the crystal lattice. The contrast mechanism will be discussed in detail in the next section.

1.4 Concept of Penetration Depth

The concept of penetration depth plays an important role in understanding X-ray diffraction topography. As X-ray penetrates into a specimen of a specific thickness, it can provide the structural information of the volume in which X-ray travels through when finally the diffracted X-ray intensity is recorded on the film. When applying different geometries during the experiment, the variation of penetration depth and its influence on the topograph must be understood.

The definition of penetration depth in X-ray Diffraction is the depth at which the intensity of incident beam reduces to 1/e.

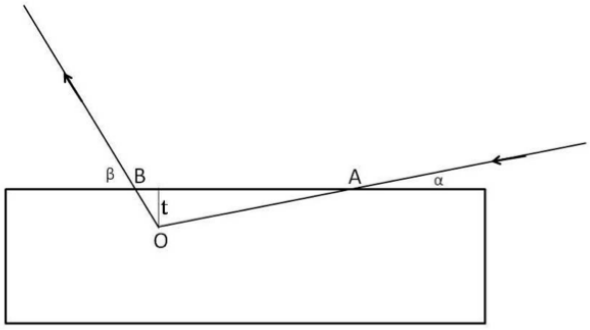

Fig.1-6 Schematic diagram for calculating penetration depth.

As shown in Fig. 1-6, the penetration depth is defined to be t, AO is the incident direction and OB is the exit direction, α and β are the incident and exit angle. Consequently, the lengths of AO and OB can be described as,

$$AO = \frac{t}{\sin\alpha}, OB = \frac{t}{\sin\beta}$$

The total path length τ of X-ray travels through the crystal is thus,

$$\tau = AO + OB = \frac{t}{\sin\alpha} + \frac{t}{\sin\beta}$$

From the definition of absorption effect of X-ray, with regard to the intensity of the incident X-ray I_0, the intensity of the exit X-ray can be described as,

$$I = e^{-\mu\tau} I_0$$

Where μ is the absorption coefficient. By the definition of penetration depth,

$$e^{-\mu\tau} = \frac{1}{e}$$

Therefore, the expression of penetration depth τ can be obtained,

$$\mu\tau = 1,$$

$$\mu\left(\frac{t}{\sin\alpha} + \frac{t}{\sin\beta}\right) = 1,$$

$$t = \frac{1}{\mu\left(\frac{1}{\sin\alpha} + \frac{1}{\sin\beta}\right)}$$

This equation, which is based on photoelectric absorption, could be used for ordinary penetration depth calculation.

For nearly defect free crystal, penetration depth is governed by extinction distance. Penetration depth z_e in this situation is given by,

$$z_e = \frac{\Lambda}{2\pi\sqrt{1-\eta^2}},$$

Where Λ is the extinction distance, η is deviation parameter (the deviation from the rocking curve peak).

1.5 Contrast Mechanism of X-ray Diffraction Topography

Defects such as dislocations, stacking faults, grain boundaries in single crystal can be imaged via X-ray diffraction topography method because the variation of diffracted X-ray intensity resulting from localized strain filed contributes to the contrast on the topograph. X-ray

topographic contrast is generally described by two mechanisms: orientation contrast and extinction contrast.

Orientation contrast is a result of inhomogeneous distribution of intensity, which is purely from the overlap and separation of diffracted X-rays. In single crystals, regional different orientations, such as grain, subgrain and twin boundaries, can give rise to orientation contrast. Orientation contrast occurs due to both the nature of X-ray and the nature of misorientation. As Fig. 1-7 shows, if either the beam divergence or the wavelength bandwidth in the incident X-ray is smaller than the misorientation between two regions (Fig. 1-7a), then only one region in the crystal can diffract at a time. Otherwise, the diffracted beams will travel along slightly different directions and produce image overlapping as they either diverge or converge. Therefore orientation contrast is presence or absence of diffracted intensity in one of the region and the degree of misorientation can thus be determined by measuring image shifts.

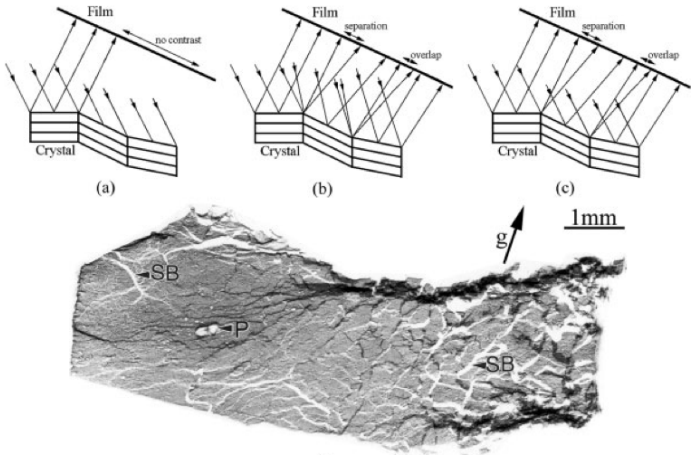

Fig. 1-7 Orientation contrast resulted from misoriented regions: (a) monochromatic radiation, beam divergence < misorientation; (b) monochromatic radiation, beam divergence = misorientation; (c) continuous radiation; (d) reflection topograph from an HgCdTe single crystal.

Extinction contrast arises from different scattering power of the region around defects and the remaining perfect crystal. The formation of the image of dislocations in topographs can be well understood by the concept of extinction contrast. There are three different types of images that comprise the dislocation image in a topograph: direct, dynamic and intermediary image due to three types of extinction contrast. In transmission geometry, absorption condition (μt) determines the type of image that can be observed, where μ is the mass absorption coefficient and t is the thickness of the crystal. Dynamical diffraction breaks down near the dislocation core where the lattice is heavily distorted compared to the rest of the crystal, and the core region thus diffracts

kinematically[18].

1.6 Motivation

Boron phosphide is a promising candidate semiconductor material for neutron detectors because of its wide band gap and large thermal neutron capture cross-section of ^{10}B. Since bulk BP is not readily available for neutron detector application, BP thin films are mainly synthesized by chemical vapor deposition (CVD). Among all the feasible substrates for BP deposition, SiC stands out due to its small lattice mismatch with BP, however it is necessary to optimize the growth condition to synthesize high quality BP thin films on SiC. In chapter III, material structure and properties of BP and growth method of BP thin films are introduced. BP thin film samples deposited on 4H-SiC and 6H-SiC under different growth conditions are characterized mainly using synchrotron X-ray topography and other techniques such as optical microscopy and scanning electron microscopy, in order to investigate the relationship between BP thin film crystal quality and substrate material and orientation and other growth conditions,

Sapphire single crystal has been widely used in high-technology industry because of its excellent mechanical properties including high strength, high hardness and also excellent chemical and electrical stability, which in total make sapphire an ideal material for optical window, substrate and construction units. It is essential to study and understand defect mechanisms in sapphire single crystal that are grown by any specific method. In chapter IV of this thesis, a-plane sapphire ribbon grown by Edge-defined Film-fed Growth method (EFG) is analyzed by characterizing the seed crystals used and the quality of as-grown ribbon, by reflection X-ray topography. Distributions and formation mechanisms of defects inside both the sapphire seed crystal and ribbon crystal are studied.

Chapter II. EXPERIMENTAL METHODS

2.1 Synchrotron X-ray Topography

Synchrotron X-ray Topography in this thesis was carried out at Brookhaven National Laboratory (BNL), National Synchrotron Light Source (NSLS), Beamline X19C, using white beam X-ray. Transmission, reflection and grazing geometries are used to investigate the overall quality of BP thin film deposited on SiC substrate. The crystal quality of single crystal sapphire grown by Edge-defined Film-fed Growth (EFG) method is characterized via transmission and reflection geometries. The schematic diagram of experimental setup that was used in beamline X-19C, BNL is shown below in Fig. 2-1. As for characterization of sapphire single crystals that have larger sizes, a scanning system was deployed in order to ensure the entire area of sapphire crystal can be covered by X-ray beam.

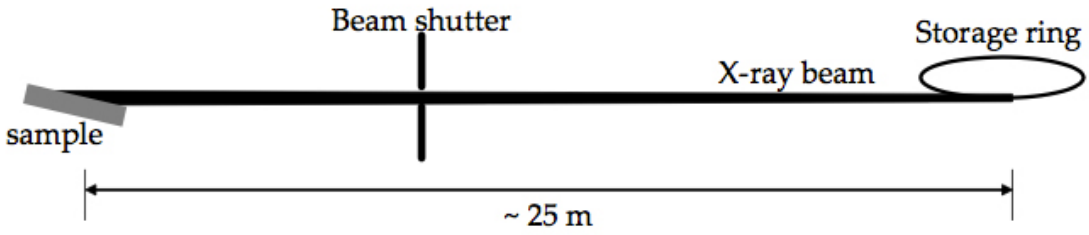

Fig. 2-1 Schematic diagram of experiment setup in Beamline X19C, BNL.

Topographic images were recorded on Agfa Structurix D3-SC. The exposure time differs from the geometries that were used, ranging from four seconds to five minutes. Based on practical experience, the exposure time varies with different kinds of materials used for experiment and with the method by which the sample is aligned for characterization. Kodak D19 developer and fixer were used to process the exposure films. After the film has been fully processed, it is then scanned by EPSON Perfection V750 PRO scanner into a digital file.

Generally, three geometries are applied for synchrotron white beam X-ray topography, i.e. transmission, reflection and grazing geometry. In transmission mode, the incident beam passes through the specimen and projects all the information of the bulk to the film placed behind the specimen, while in reflection geometry, the diffracted beam reflects onto a film set in front of the specimen. Grazing geometry can be regarded as a type of reflection geometry set at small incident angle (typically $< 10°$), thus resulting in low penetration depth and could reveal most defect information on the specimen surface. Schematic diagrams of three geometries are shown

below.

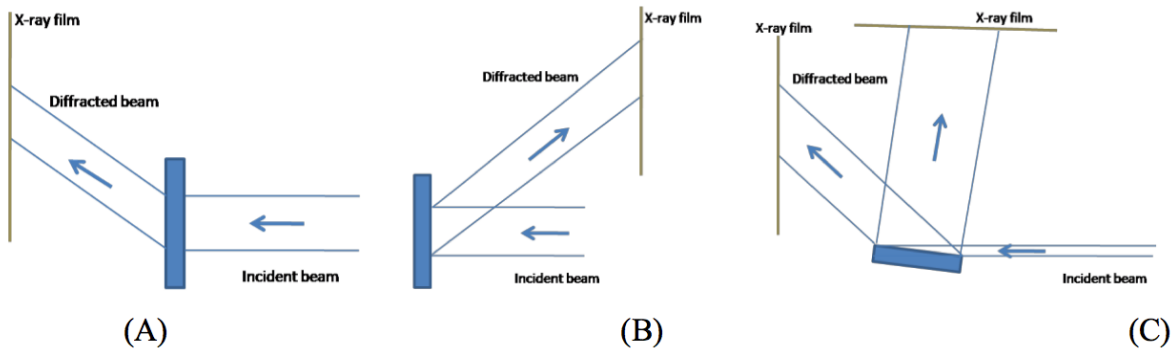

Fig. 2-2 Schematic diagrams of three geometries in XRT. (A) Transmission geometry, (B) Reflection geometry, (C) Grazing geometry.

2.2 Scanning Electron Microscopy

In order to characterize single crystal thin film quality, Scanning Electron Microscope (SEM) was used to investigate the surface morphology of the specimen. Unlike optical microscope, a scanning electron microscope uses electrons as the "light source". SEM can achieve a high resolution of 1 nm. There are two types of electron guns: thermionic gun and field emission gun. Electrons that generated from the electron gun then get accelerated and focused to impinge on the specimen, with a normal spot size of less than 10 nm. When electron beam collides with atoms in the specimen, different types of signals are generated; two most common signals are backscattered electrons (BSE) and secondary electrons (SE)[19].

Backscattered electrons are beam electrons that escape from the entrance surface after undergoing elastic scattering with atoms (normally nuclei), while secondary electrons are those undergoing inelastic scattering with the outer shell electrons. As a result, BSE signals are used for identifying the chemical composition on the specimen surface, while SE signals are used to detect the surface morphology. Schematic diagrams of elastic and inelastic scattering are shown in Fig. 2-3.

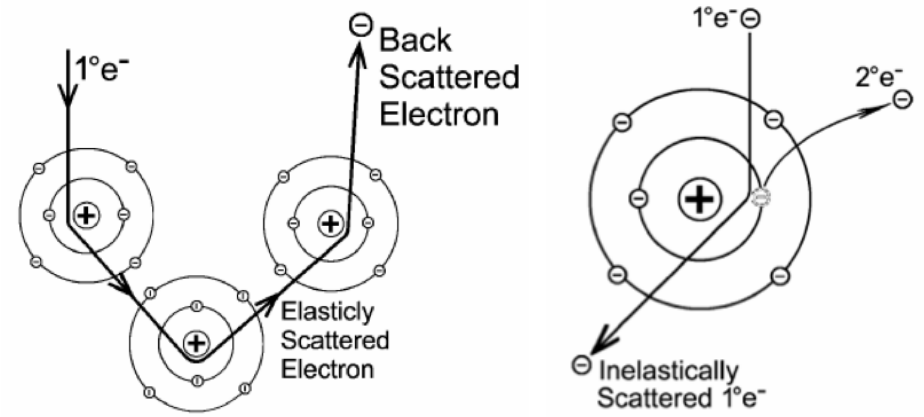

Fig. 2-3 Schematic diagrams of elastic scattering (left) and inelastic scattering (right) of interaction between electron beam and the atom.

In this thesis, the SEM experiments are carried out in Department of Materials Science & Engineering, SBU, using the model LEO 1550. BSE and SE modes are employed to investigate the surface morphology of boron phosphide epitaxial thin films.

Chapter III. CHARACTERIZATION OF BP THIN FILMS ON SiC

3.1 Chemical Vapor Deposition

Chemical vapor deposition (CVD) is the one of the reported methods used to deposit BP thin films[20]. Silicon is the most common substrate for epitaxial BP film growth and silicon carbide as the less common substrate material. The deposition of BP thin film is carried out in a gas flowing system, the deposition chamber is demonstrated in Fig. 3-1. The thermal decomposition of diborane-phosphine (B_2H_6 – PH_3) or the thermal reduction of boron tribromide-phosphorous trichloride mixtures in a hydrogen atmosphere are the two reactions used for BP deposition.

$$B_2H_6 + 2PH_3 \xrightarrow{Heat,H_2} 2BP + 6H_2$$

$$BBr_3 + PCl_3 + 3H_2 \xrightarrow{Heat} BP + 3HBr + 3HCl$$

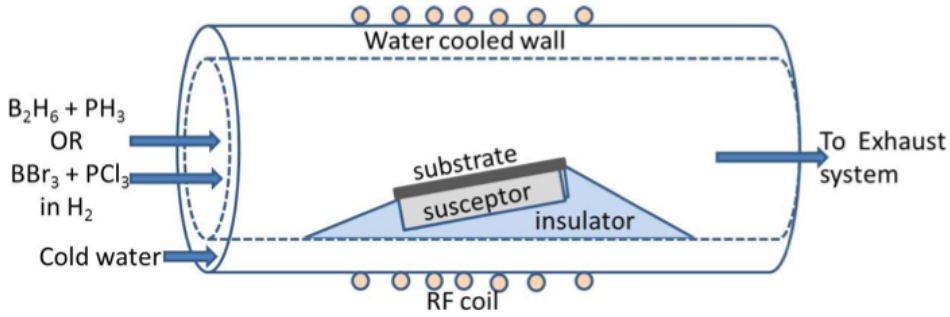

Fig. 3-1 Schematic of deposition chamber for BP thin film growth

As shown above, the reactants of specific composition are passed into a silica tube, which is water cooled in order to minimize the influence of gas-phase reaction. The RF coil around the reaction tube can heat up the boron phosphide coated graphite susceptor on which is the silicon carbide substrate. The substrate temperature is held at about 900°C in hydride reaction and 850°C-1250°C in halide reaction. It is essential that the phosphorus partial pressure must be kept higher than BP vapor pressure to ensure desired formation of BP but not $B_{12}P_2$, which would reduce the crystalline uniformity and affect electrical properties[21].

In this chapter, all the boron phosphide thin film samples are grown by the research group led by Professor. James Edgar from Kansas State University under different conditions with the choice of 4H-SiC and 6H-SiC as substrates. The information of different specimens on different

substrates and growth condition are listed in the table below. In the next section, thin film crystal quality of samples with different substrates and growth conditions are characterized and compared by optical microscopy, synchrotron X-ray topography as well as scanning electron microscopy and the optimum combination of substrates and growth conditions is discussed.

Tab. 3-1 Information on different substrates, growth condition and P/B ratio used for different samples

Sample Number	Substrate	Growth Condition	Phosphorous/ Boron Ratio
BP45	4H-SiC		10
BP48			10
BP70		1250°C, 3 Hours	100
BP46	6H-SiC		10
BP47			10
BP61		1250°C, 90 minutes	1000

3.2 Experimental Data Analysis

3.2.1 Off-cut Measurement by Synchrotron XRT

In order to determine the off-cut direction and magnitude of each sample synchrotron X-ray topography was carried out after (0001) basal plane of each sample is placed perpendicular to the X-ray beam by laser alignment. The exposure time for off-cut measurement was five seconds in order to reduce interference of the direct beam which would darken the overall background. Specimen-to-film distance was set to be 100 mm so that a specific diffraction pattern can be identified with much more certainty. The size of X-ray beam was confined to $1\,mm \times 1\,mm$ so that the distance for identifying two close diffracted spots can be minimized. The diffraction patterns were then compared with patterns simulated by LauePt program therefore the off-cut magnitude and direction can be determined.

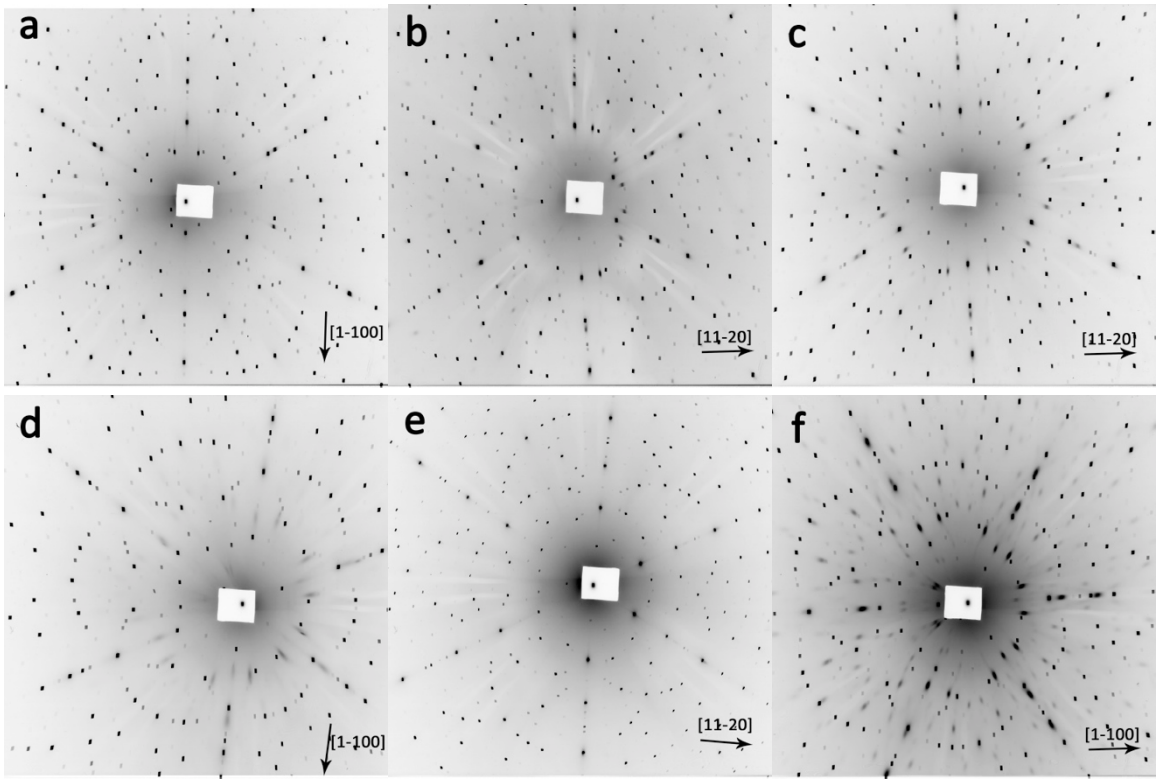

Fig. 3-2 Tansmission topographs of off-cut measurement. (a) BP45; (b) BP46; (c) BP47; (d) BP48; (e) BP61; (f) BP70.

The transmission X-ray topographs of all samples are shown in Fig. 3-2, the pattern deviation from standard six-fold-symmetry pattern results from the off-cut angle between (0001) basal plane and surface plane. It can be preliminarily concluded that those well-defined spots with darker color that indicate a higher diffracted intensity come from SiC substrate, while those blurry and distorted spots probably come from the epitaxial layer. Among the six patterns Fig. 3-2f exhibits entirely darkest spots (highest intensity) likely as a result of a thicker substrate and epilayer. Further confirmation in standard (0001) plane topographs is needed.

After matching diffraction patterns with simulated patterns in LauePt program, the magnitude and direction of each sample's off-cut can be identified, as listed in Tab. 3-2. Off-cut angles mostly differs between 3° to 5° along the directions of [1-100] or [11-20], sample BP47 has no off-cut angle, which means sample surface plane normal is [0001] (C-axis) and thus marked "on axis".

Tab. 3-2 Magnitude and direction of each sample's off-cut

Sample Number	Substrate	Off-cut magnitude	Off-cut direction
BP45	4H-SiC	4.37°	[1-100]
BP48		1.62°	[1-100]
		2.88°	[11-20]
BP70		4°	[1-100]
BP46	6H-SiC	5°	[11-20]
BP47		On axis	
BP61		3.75°	[11-20]

3.2.2 Optical Microscopy Results

Information on magnitude and direction of (0001) plane tilt to surface plane can be determined through off-cut measurement, so does the orientation of each sample, which is regarded as an essential reference during the subsequent optical microscopy, SEM and synchrotron X-ray experiment.

In order to obtain preliminary surface morphology information, optical microscopy is used as a complementary method besides SEM. The optical image of each specimen is presented below. All the specimens are placed in the same orientation as in SEM imaging.

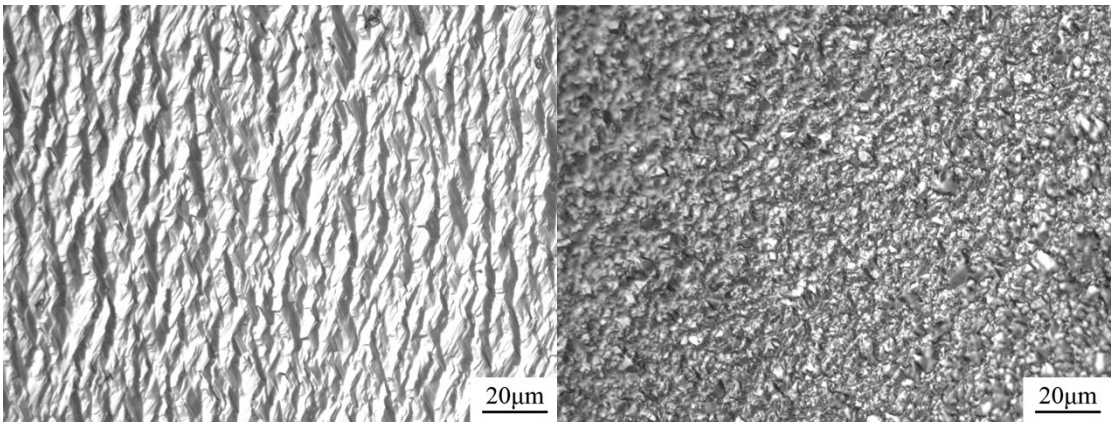

(a) BP45 (b) BP 48

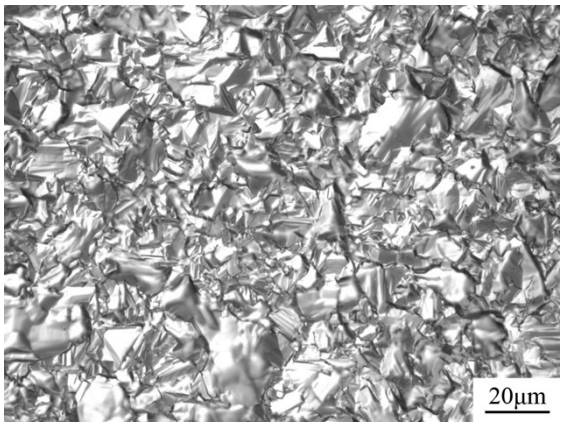

(c) BP70

Fig. 3-3 Optical images of all samples on 4H-SiC substrate.

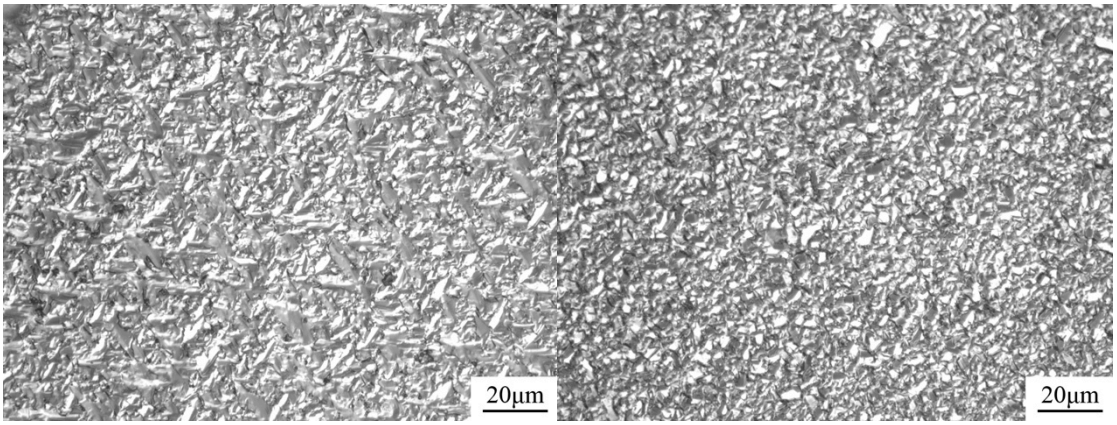

(a) BP46 (b) BP47

Fig. 3-4 Optical images of all samples on 6H-SiC substrate.

From Fig. 3-3 and Fig. 3-4, it can be concluded that among all the samples BP45, BP70 and BP46 exhibit obvious triangular features, which are strong evidence of cubic BP crystal. While surface optical images of BP48 and BP47 show that the grain size of the epitaxial film is much smaller than that of other samples', with no crystalline features being seen. A number of crystalline features can be identified in sample BP46, which makes it better in crystal quality in comparison with sample BP47, where no obvious triangular features can be distinguished, which means that crystal structures are not uniform, or lack of evidence of single crystal cubic boron phosphide by optical microscopy. Based on the optical microscopy results, BP45, whose substrate is 4H-SiC, can be determined as the best-quality sample since it has the most uniformly distributed 60° and 120° features on a smoothest surface.

3.2.3 Synchrotron White Beam X-ray Topography Results

To study crystal quality of the epitaxial film and figure out its orientation with regarding to the substrate, SWBXT technique was carried out, using the transmission geometry, which means (0001) basal plane of SiC is perpendicular to the incident beam, with the exposure time of five minutes. The extended exposure time compared with that in off-cut measurement is to ensure the formation of low-intensity diffracted spots from small quantities of other possible compounds, such as $B_{12}P_2$. The beam size was adjusted, like that in off-cut measurement, to be 1mm × 1mm. In this way, diffracted spot from each lattice plane in either epitaxial film or substrate with a distinguishable intensity could be recorded on the photographic film simultaneously.

As a result, the orientation relationship, relative amount and crystal quality of each component can be identified by matching the diffraction pattern with every simulated pattern of the component that could possibly exist in the specimen (in this case: SiC, BP, $B_{12}P_2$). Transmission topographs of all 4H-SiC samples are shown below.

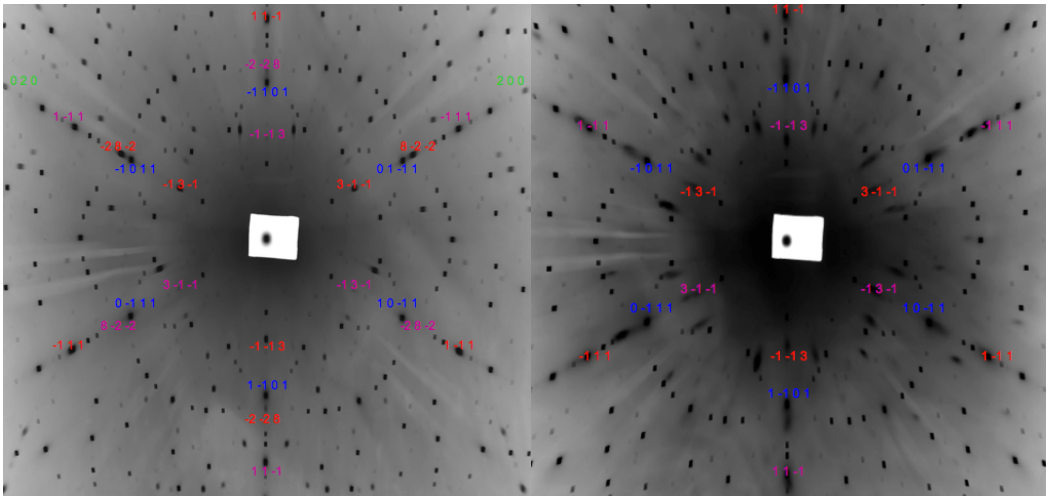

(a) BP45 (b) BP48

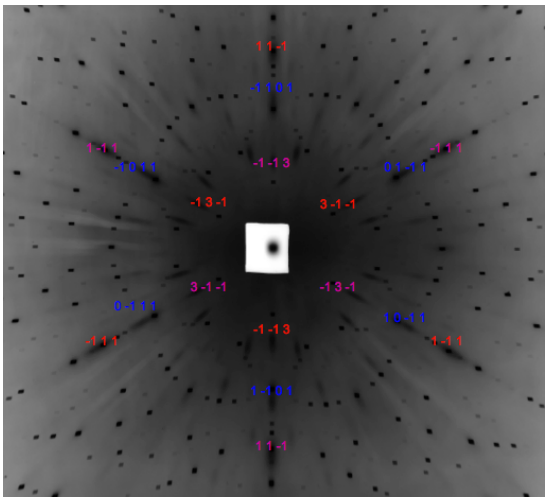

(c) BP70

Fig. 3-5 Transmission topographs of (0001) basal plane of all 4H-SiC samples, with side planes set to be (11-20). Blue: 4H-SiC; Red: BP; Pink: BP twin; Green: $B_{12}P_2$

All transmission topographs were recorded with (0001) basal planes of SiC aligned normal to the incident beam and (11-20) aligned horizontally. Consequently, a six-fold-symmetry diffraction pattern is exhibited in each topograph, since the c-plane (0001) of SiC consists of silicon/carbon hexagons. As shown above, most diffracted spots in the topograph have sharp edges and a well-defined shape and are shown to be diffraction patterns from 4H-SiC after matching with simulated (0001) 4H-SiC pattern. Besides, there are a number of distorted spots with blurry edges that don't belong to SiC pattern, however, a good match between distorted spots and the simulated pattern of (111) BP diffraction with a (1-10) side plane has been identified, which indicates that the stacking relation between the epitaxial BP thin film and SiC substrate is: (0001)/[11-20]-SiC//(111)/[1-10]-BP. The simulated diffraction patterns of (0001)-SiC_{4H} and (111)-BP are demonstrated below (Fig. 3-9) for comparison.

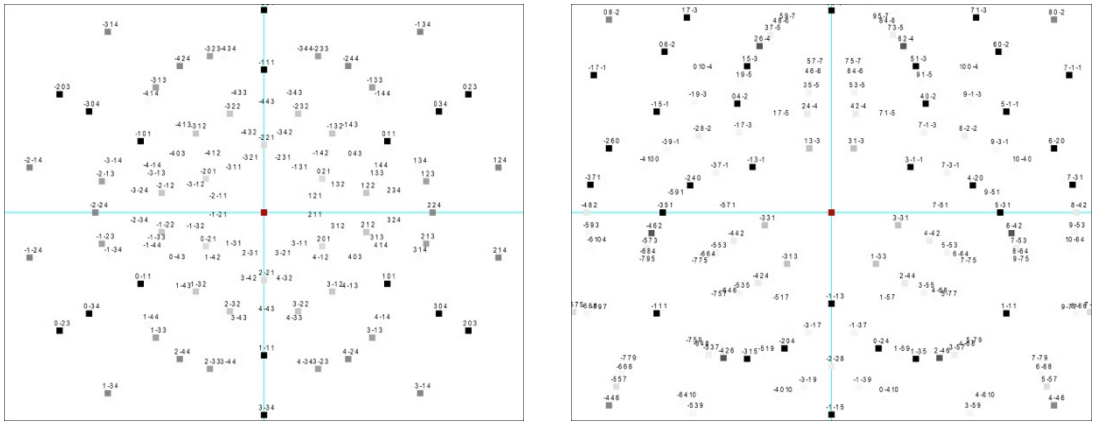

Fig. 3-6 Simulated patterns of (0001)-4H-SiC (left) and (111)-BP (right).

The simulated (111)-BP pattern is shown in the above (Fig. 3-6 right), however it is observed that the simulate BP pattern which consists of strong spots does not perfectly coincide with the pattern that consists of blurry unidentified spots in terms of relative intensity. For example in Fig. 3-5b, there exist two blurry but strong spots on each side of (3-1-1)-BP, which has been marked red upon the (111)-BP diffraction pattern. Same spots also emerge in the twinned (111)-BP, thus all of these unusual spots compose a six-fold-symmetry pattern. After matching with the simulated (111)-BP pattern in detail, it can be figured out that the two unusual blurry spots match well with twinned (4-42)-BP and twinned (2-44)-BP spots. The reason of the difference between diffracted intensity and simulated intensity result from the deviation between the actual structure of BP and the standard structure of cubic BP. It is probable that point defects such as anti-structure defects of boron and phosphorous atoms are contained in the BP epilayer, which remains to be investigated.

In Fig. 3-5a, it can be figured out that distorted spots with relatively high intensity generate a three-fold-symmetry pattern that coincides with (111)/[1-10]-BP pattern, while an opposite-oriented pattern with relatively low intensity can be identified and is marked as red. Based on the principles of X-ray diffraction and the structure of cubic BP, it can be proved that the low-intensity ill-defined patterns result from twinned BP crystal. As for the deposition of BP on SiC substrate, crystallites with two opposite orientation can be deposited with equal chance and form a twinned structure with the twin axis being the same as BP (111) plane normal. As in the topograph, the twinned (111)-BP pattern is a product of 180° rotation about [111] of the original (111) BP diffraction pattern, as marked in purple.

In comparison with BP45, topographs of BP48 (Fig. 3-5b) and BP70 (Fig. 3-5c) exhibit a remarkable increase of diffracted beam intensity as each spot becomes darker, which is probably due to the difference in the thickness of both the epilayer and the substrate. Sample BP70 and BP48 might have a much thicker substrate and BP film than sample BP45. In addition, the distortion of twined and untwinned BP spots in Fig. 3-5b and 3-5c is much more that in Fig. 3-5a. This could lead to the conclusion that BP epilayers in sample BP48 and BP70 have much more in-plane stress compared with BP45, which cause the diffracted beam distort more severely, in other word, sample BP45 exhibits the best crystal quality in the aspect of growth stress that resulted from imperfect growing conditions.

Another significant difference that lies among three samples is the relative diffraction

intensity between (111)-BP and twined (111)-BP. As shown in Fig. 3-5b, c, the intensities of diffracted spots from twinned (111)-BP are significantly higher than that in Fig. 3-5a and even reach the same level as that of spots from untwinned (111)-BP, resulting in an obvious six-fold-symmetry pattern superimposed on the (0001) diffraction pattern from SiC substrate. The increase in the twinned (111)-BP diffracted beam intensity provides a strong evidence for an increase in the relative amount of BP twin crystals, thus leaving a negative influence on the crystal quality of the specimen. The larger the portion of twinned BP crystals becomes, the worse the crystal structure uniformity will be.

Fig. 3-7 shows (0001) transmission topographs of all samples with 6H-SiC substrate in order to compare the crystal quality with all 4H-SiC samples. (11-20) plane is aligned horizontally as the side plane in all of the 6H-SiC samples. The common feature in the three diffraction patterns below is that all distorted and blurry diffracted spots display obvious six-fold-symmetry patterns, which are confirmed to be a sum of the (111)-BP and twinned (111)-BP diffraction patterns. Besides, the difference between the intensity of twinned and untwinned BP patterns is quite little since the darkness of the two is nearly the same, which indicates that crystal structure uniformity is not sufficiently good.

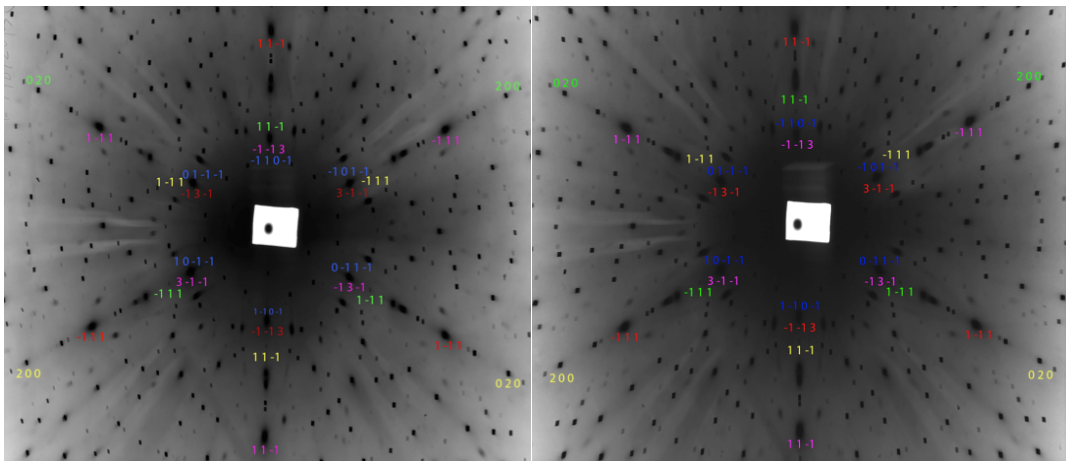

(a) BP46 (b) BP47

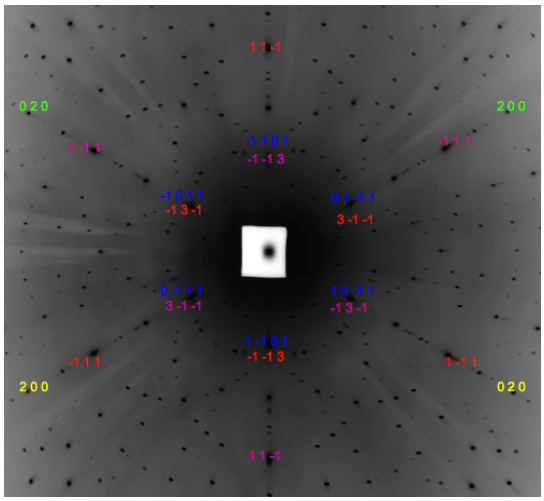

(c) BP61

Fig. 3-7 Transmission topographs of (0001) basal plane of all 6H-SiC samples, with side planes set to be (11-20). Blue: 4H-SiC; Red: BP; Pink: BP twin; Green: $B_{12}P_2$; Yellow: $B_{12}P_2$ twin.

Another significant distinction between topographs of 4H-SiC substrate and 6H-SiC substrate arises in the additional presence of unidentified distorted spots in the 6H-SiC substrate topographs that also composes a six-fold-symmetry pattern. After comparing the diffraction pattern with simulated (111)-$B_{12}P_2$ pattern ((1-10) as side plane), a well match is obtained between the unidentified distorted spots and those highest-intensity spots such as (200), (020), (002), as shown in Fig. 3-8. The presence of the six-fold-symmetry unidentified pattern is the very evidence of the existence of (111)-$B_{12}P_2$ twin. Each of the highest-intensity spot from $B_{12}P_2$ finds its counterpart in the other position that is symmetric to the topograph center. Consequently the untwinned $B_{12}P_2$ and twinned $B_{12}P_2$ are marked as green and yellow respectively. Other spots from $B_{12}P_2$ with high intensity such as (11-1), (-111) and (1-11) are found to be overlapped either by high-intensity spots from BP or by the dark background generated by the direct beam, however it is still of high possibility that (111)-$B_{12}P_2$ and its twin come into existence based on the principles of deposition of BP on SiC. The appearance of $B_{12}P_2$ in each of the 6H-SiC sample acts as a strong proof for the result that the crystal structure uniformity in 6H-SiC samples is not so good. The CVD-deposited BP samples are an integration of (111)-BP, twinned (111)-BP, (111)-$B_{12}P_2$ and twinned (111)-$B_{12}P_2$, which would definitely degrade the BP thin film performance in aspects of physical, chemical and electrical properties.

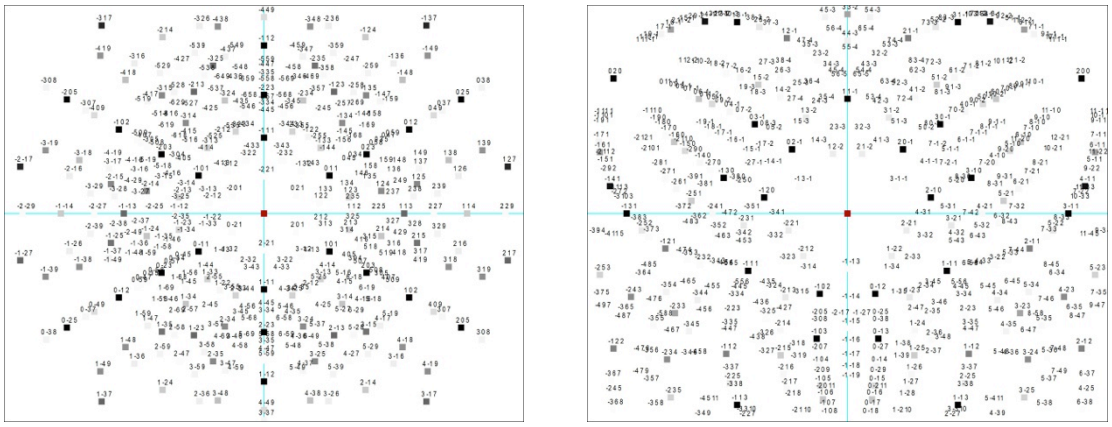

Fig. 3-8 Simulated patterns of (0001)-6H-SiC (left) and (111)-BP (right).

As in all the topographs of 4H-SiC substrate (Fig. 3-5), the appearance of $B_{12}P_2$ spots is only found in sample BP45. The two highest-intensity spots are marked as green in the topograph. No blurry spots are found at the opposite center-symmetric position, which means that no (111)-$B_{12}P_2$ twins are generated during the growth. Meanwhile, No strong evidences on the presence of $B_{12}P_2$ are found from topographs of BP48 and BP70.

Fig. 3-7 also provides the information on comparison of relative intensity and relative strain in distorted spots from different samples. Intensity of the diffracted spots in topographs of BP46 and BP47 are nearly the same, while the diffracted beam intensity from sample BP61 is significantly lower than the other two, most probably due to the relatively thinner substrate and epilayer. The distortion difference of the pattern of sample BP46 and BP47 can be hardly distinguished, however, the distortion of the diffracted spots in BP61 is found to be larger since the distorted spots have been transformed into a needle-like shape, which represents a highly strained epitaxial BP film.

Furthermore, X-ray topography in reflection and grazing geometry of experiments on different samples provides useful information on crystal structure of the epilayer, for the reason that the penetration depth of X-ray is much smaller in these two geometries. It's been a powerful technique to evaluate the crystal quality of any epitaxial structures. In the reflection geometry experiment, the incident angle was set to be 5° and the exposure time was five seconds. An exactly same series of blurry and distorted spots are found in each sample's topograph, however, it cannot provide any other useful information beyond the fact that these blurry spots don't belong to SiC but BP. In this section, the reflection geometry remains a supplementary technique to confirm the correct surface on which BP film is deposited.

During the grazing experiment session, several selected samples were characterized by grazing geometry and the topographs are shown below in Fig. 3-9. The grazing incident angle between the X-ray beam and the sample surface was set to be 2°, and the film-to-specimen distance was set to be 30 mm. Unlike the off-cut measurement, the X-ray beam size in grazing geometry was adjusted to the size that just completely covers the sample so that the overall information on or near the surface of the sample can be revealed. The exposure time was tentatively set to be five seconds to check if diffracted spots from BP could appear.

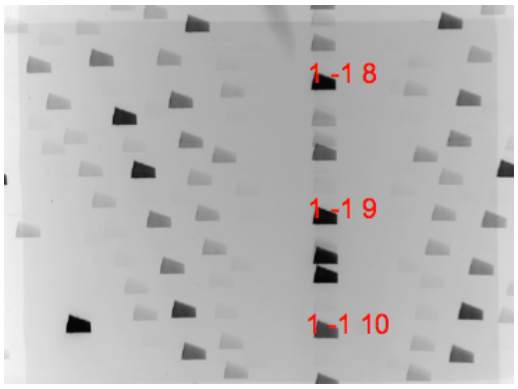

(a) BP45 (4H-SiC)

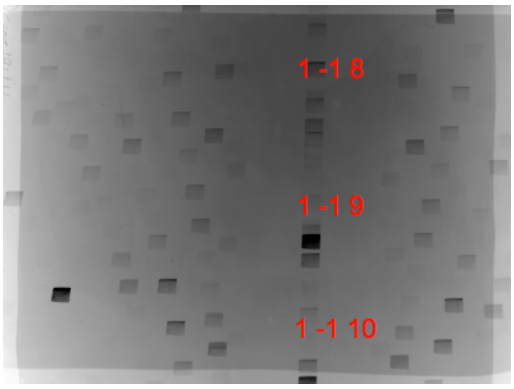

(b) BP70 (4H-SiC)

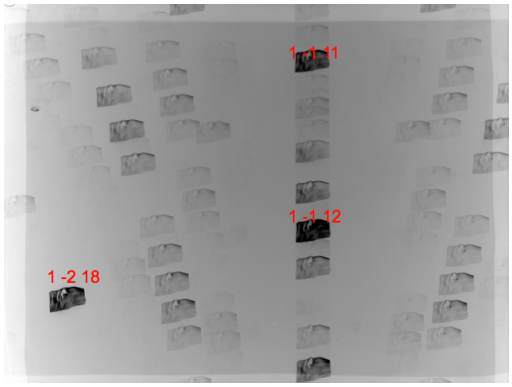

(c) BP61 (6H-SiC)

Fig. 3-9 Grazing-incidence topographs of different samples.

As shown in the figures above, the diffraction patterns are mostly composed of those sharp spots with well-defined edges. After each image is enlarged so as to compare every sharp-edge spot, it can be seen that each spot reveals same defect characteristics like white circular spots with dark borders as in BP45 and BP70, which are results from screw dislocation and localized weakened diffracted beam intensity presented as white lines in BP61. In addition, a moderately good match with simulated SiC patterns for those solid and sharp spots has been obtained via the

LauePt program, with some representative indexes marked in each figure. All these evidences draw a conclusion that most of solid spots originate from SiC substrate, however, the relative intensities of several spots do not match with the simulated pattern, the reason of which remains to be investigated. Besides, there seems to exist two or three blurry spots with very low intensity in the topograph of BP45. It cannot be confirmed that whether these unusual spots belong to SiC or BP, after no good matches between the two are found. The simulated patterns of SiC and BP within the corresponding area with diffraction patterns are shown below for comparison. The inconsistency between the relative intensity of simulated spots and that of diffraction pattern can be seen, the reason for which is probably the short exposure time that couldn't make each diffracted spots appear or gain enough contrast on the topograph.

Fig. 3-10 Simulated patterns of 4H-SiC (left) and 6H-SiC (right) in grazing geometry.

Since each spot in the topographs above represents a set of atomic planes and is a projection of the whole sample surface, information on differences between the diffracted spot area and sample surface area can be obtained. As in Fig. 3-9a and 3-9b, the areas of diffracted spots are more or less the same and are quite similar to the actual sample surface areas. Surprisingly, the areas of diffracted spots in Fig. 3-9c (BP61) are nearly five to six times larger than the actual sample surface area, and the actual size of BP61 is about 2/3 of the size of BP45 and BP70. The reason for this magnification effect on surface area can be attributed to the strain in the SiC substrate, since each spot originates from SiC. As X-ray interacts with the SiC substrate and gets scattered, it could either form a convergent or a divergent diffracted beam because of the inhomogeneity in the crystal structure, for example, X-ray could change its direction during the interaction with the local strain field that exists in the sample, which can be generated from dislocations, inclusions and other crystal defects. The final contrast on the topograph will thus be changed. In this case, the phenomenon of enlarged diffracted spots thus reaches the conclusion that the 6H-SiC substrate of BP61 is highly strained and also reveals significantly higher dislocation density than other two selected samples, which would potentially degrade the crystal

quality of epitaxial BP film.

3.2.4 SEM Results

With the information on orientation relationship between the substrate (4H-SiC or 6H-SiC) and epitaxial BP thin film obtained from SWBXT results, surface morphology information under a higher magnification and a higher resolution can be acquired by using SEM method in the condition that all samples are placed along the same orientation. Fig. 3-11 in the above shows the SEM images of samples with different substrates (4H-SiC or 6H-SiC), which are all taken in secondary electron mode as sophisticated surface structures are presented under desired magnification. Some representative features like 60° and 120° angles that are evidence of BP crystals and its twins are marked red in each images. Among all these samples, BP61 exhibits inhomogeneous surface morphology (as demonstrated in Fig. 3-12) even when examined by human eye, as a result, BP61 has been marked into three parts and has been analyzed in SEM respectively.

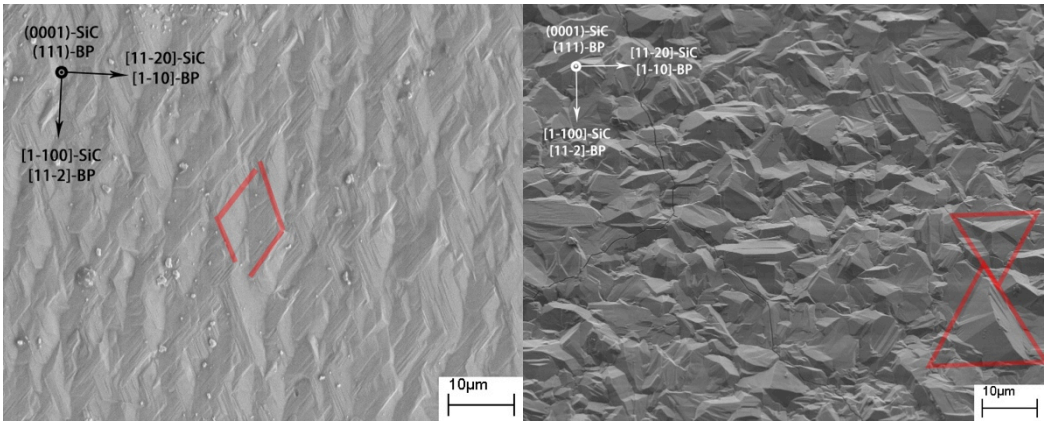

(a) BP45 (4H-SiC) (b) BP70 (4H-SiC)

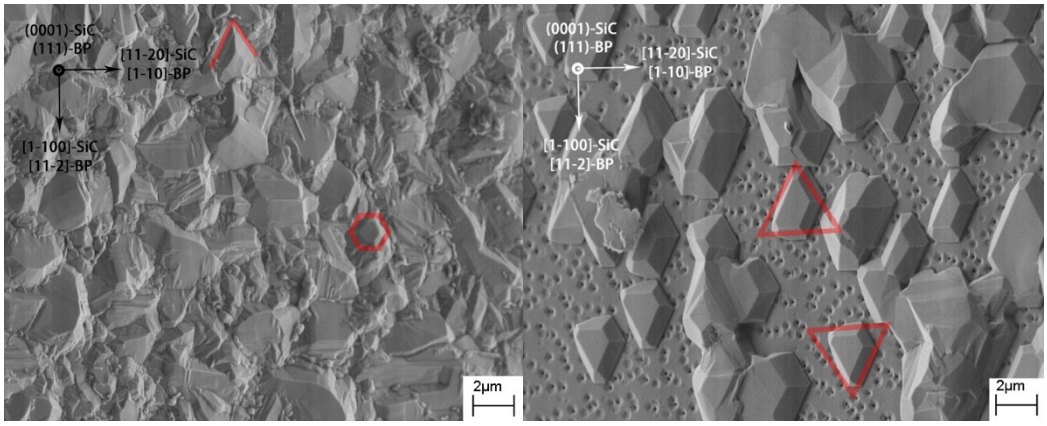

(c) BP47 (6H-SiC) (d) BP61-I (6H-SiC)

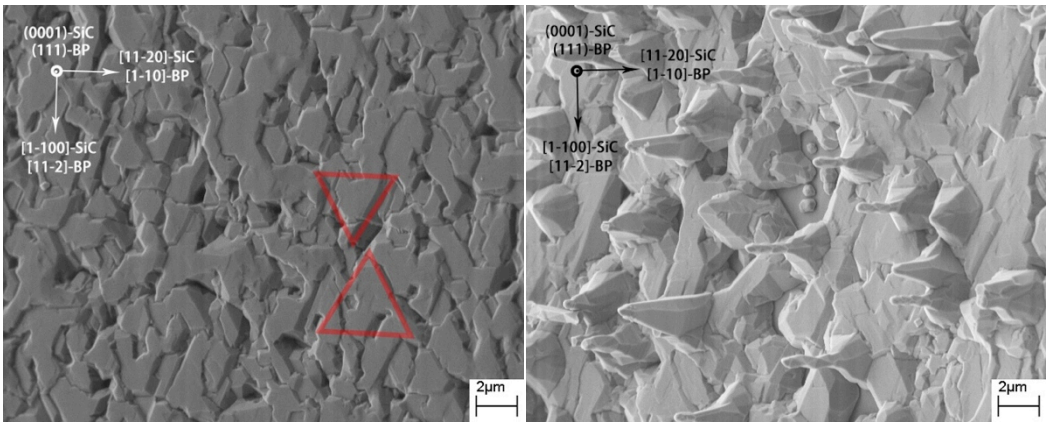

(e) BP61-II (6H-SiC) (f) BP61-III (6H-SiC)

Fig. 3-11 SEM images of samples with different substrates.

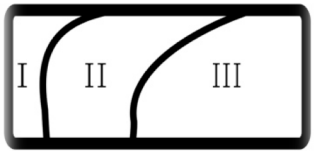

Fig. 3-12 Schematic of inhomogeneous surface area in sample BP61.

It is not a surprising result for the SEM analysis as shown in Fig. 3-11 since optical microscopy has been carried out under a slightly lower magnification (500X) except for several details that emerge because of the high resolution of SEM. As in Fig. 3-11b and 3-11c, the crystal uniformity is not as good as that of BP45, which possesses a relatively smooth surface contains high crystalline features of normalized angles and edges. While on surface of BP70 and BP47, obvious evidence that two opposite-oriented BP crystallites coexist are figured out, as marked in the images. These features are results from simultaneous growth of (111)-BP and twinned (111)-BP crystallites. As presented, SEM image of BP67, whose substrate is 6H-SiC, has relatively rougher surface than BP70 and shows less crystalline features, except for two marked evidences of twinned and untwinned BP crystals. Surprisingly, one nanoscale crack with a width up to several hundred nanometers has been found throughout the SEM image. It can be a strong evidence of high strain that exist in epitaxial BP thin film, with the energy released in form of microcracks. It can be predicted from Fig. 3-11b that the growth condition might not be optimized since cracks are presented on the sample surface, which may due to a over-thick BP thin film as the deposition time period is too long.

From SEM images in Fig. 3-11d, e and f, the overall surface morphology information of BP61

can be obtained. In each figure, obvious evidences of crystalline features like sharp edges and consistent angles are shown, especially in section I of BP61, where a large portion of twinned (111)-BP are visible. Additionally, several crystal facets on each individual BP crystallites are shown under this magnification and nearly half of the analyzed area is barely covered with BP. While in section II, a relatively thicker BP film with sharp edges and normalized angles is presented, however in section III, a number of separated BP crystallites are deposited on top of a flat surface, with a sharp-pointed peak sit in the center of each island. Elemental analysis in SEM shows that all these peaks are rich in phosphorous. The mechanism of this growth phenomenon has not been understood yet, however it can be predicted based on the growth conditions of each sample that it might be related to the high phosphorous/boron ratio that was used during the CVD growth. The inhomogeneity in surface morphology of sample BP61 might be because of the unstable growing parameters during CVD and variation in local growth environment. Most likely, the poor crystalline quality could be attributed to the low quality of the 6H-SiC substrate that was used, as plenty of dislocations and grain boundaries are observed in the grazing geometry X-ray topography.

3.3 Discussions

Results from off-cut measurement using transmission X-ray topography provide the information on magnitude and direction of each sample. Meanwhile, by using transmission X-ray topography, the relations of crystal orientations of SiC substrate and BP single crystal film can be figured out. Consequently, combination of this information can reveal the nature of both structures of SiC substrate and its correlated epitaxial BP film. Schematics of atomic structures of selected samples are shown below (Fig. 3-13). The blue atoms stand for silicon and the black stands for carbon. The side view of the SiC substrate only shows the top four or five atomic layers instead of the full range of a unit cell of 4H/6H-SiC, which is more convenient for demonstration.

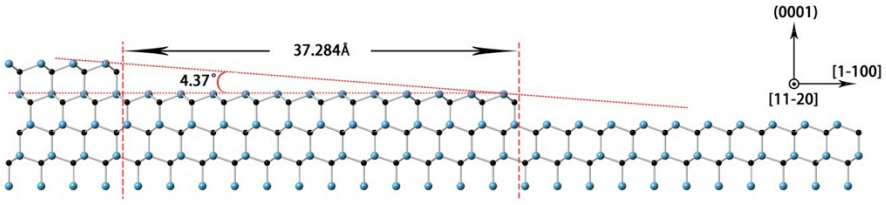

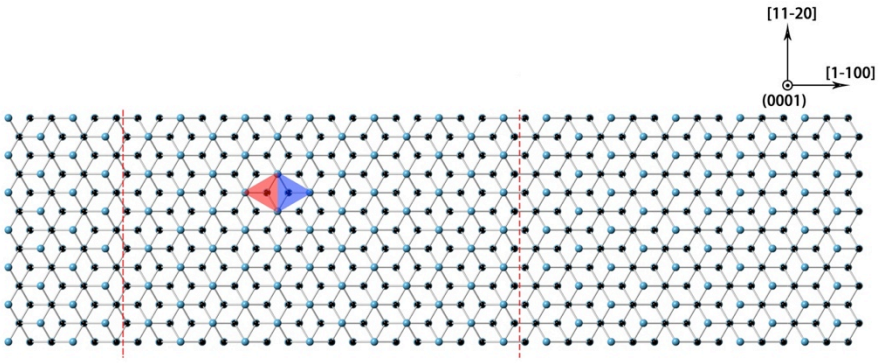

Fig. 3-13 Atomic structures of sample BP45 along [11-20] direction (top) and [0001] direction (bottom).

Sample BP45 has an off-cut angle of 4.37° along [1-100], and the length of the terrace on (0001) basal plane after inclining 4.37° to the sample surface is measured, in CrystalMaker program, to be 37.284 Å, or equals to 12 layers of $d_{(3\text{-}300)}$. Each step is of the same length so as to compensate the off-cut angle. As in the substrate atomic structure of BP70, which has an smaller off-cut angle of 4°, the length of each terrace is therefore increased to 40.391 Å, or equals to 13 layers of $d_{(3\text{-}300)}$, as shown in Fig. 3-14. From the top view of the (0001) basal plane of 4H-SiC substrate (as in Fig. 3-14 bottom), the six-fold construction of silicon and carbon atoms are easily seen, which is the essence of the six-fold-symmetry diffraction pattern. Based on the orientation relation between SiC substrate and BP epilayer, the nucleation sites for growth of boron phosphide thin film can be presented along this viewing direction. The bond length of B-B is 3.209 Å, which has a mismatch as small as 4.4% with the bond length of Si-Si (3.073 Å) on the Si-face of 4H-SiC. As labeled red and blue on top of (0001) basal plane in Fig. 3-14, the triangular configurations of boron atoms stands for the original nucleation site for BP deposition. Two opposite-oriented BP crystals are thus generated when boron triangle sits on the hexagonal Si face of the SiC substrate. This is also in perfect agreement with the SEM results where rhombohedral features along [1-100] direction has been figured out. One can also conclude from the schematic that the length of each terrace has been long enough to make the simultaneous nucleation of (111)-BP and twinned (111)-BP crystallites feasible. If we take SWBXT results of all samples into account, BP45 is undoubtedly the one with best crystal quality, since the weakest intensity from twinned (111)-BP is presented.

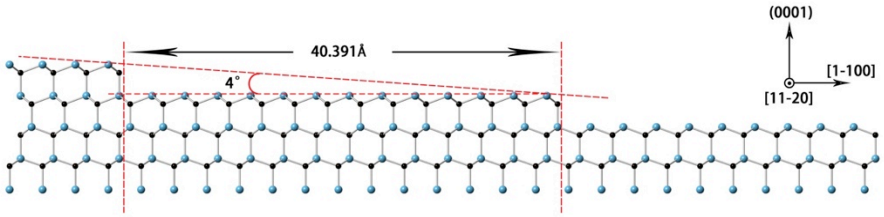

Fig. 3-14 Atomic structure of substrate of BP70 along [11-20] direction.

Based on all the experimental results above, it can be similarly concluded that the off-cut magnitude and direction differences in this patch of samples would leave little influence on the crystal structure uniformity. The reason is that even on the narrowest (0001) terrace in the 5°-off-cut sample there're more than enough possibilities for (111)-BP and twinned (111)-BP to nucleate at the same time. As the SWBXT results shows, each topograph shows some distinguishable diffracted spots that coincide with BP diffraction pattern. In addition, no obvious differences between crystal quality in off-axis sample and on-axis sample can be figured out.

The substrate atomic structure of BP46 (6H-SiC) is shown below for comparison for the reason that it has an alternative substrate (6H-SiC) and an off-cut along a different direction with the highest magnitude (5° off-cut). The length of the (0001) terrace in BP46 is 29.194 Å, or equals to length of 19 layers of (22-40) plane.

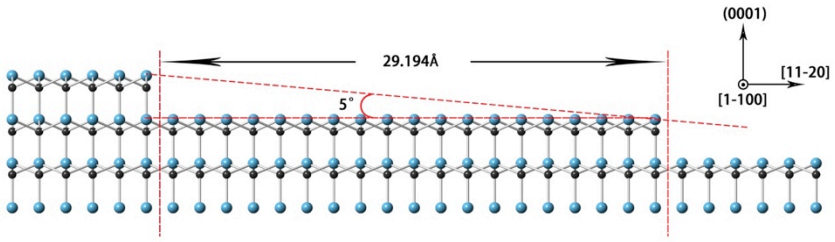

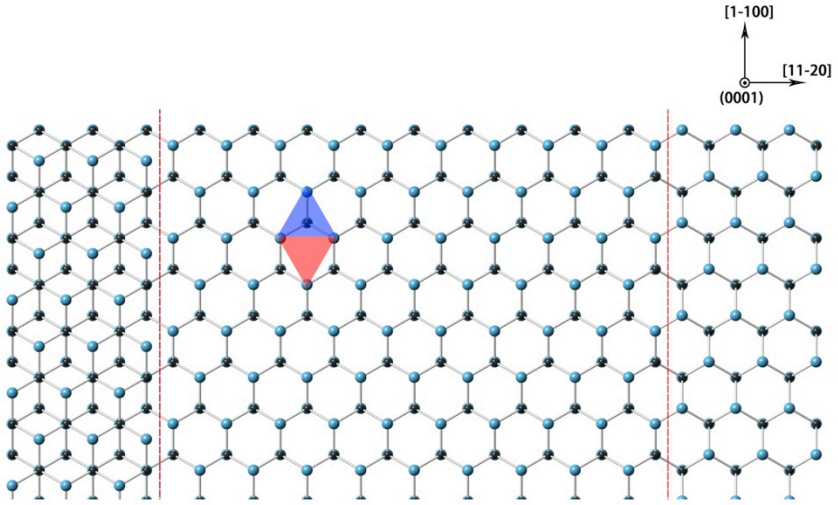

Fig. 3-15 Substrate atomic structure of BP46 (6H-SiC) along [1-100] direction (top) and [0001] direction (bottom).

3.4 Conclusions

In this chapter, material structure and properties of boron phosphide (BP) was introduced, so was the process of Chemical Vapor Deposition method for synthesis single crystal BP film on SiC substrate. A batch of BP thin film samples with different substrate and under different growth conditions was analyzed by different characterization methods including optical microscopy, scanning electron microscopy and synchrotron X-ray white beam topography.

The crystal quality of samples with 4H-SiC substrates is comprehensively better than samples with 6H-SiC substrates, mainly because of the absence of diffracted spots from (111)-$B_{12}P_2$ and twinned (111)-$B_{12}P_2$. Samples with an off-cut angle between (0001) basal plane and sample surface (for example, BP46) possess quite similar crystal quality compared with the on-axis sample (BP47), based on the evidence that BP47 and BP46 exhibits nearly the same intensity of twinned (111)-BP and (111)-$B_{12}P_2$ and also the same amount of distortion of these diffracted spots. In addition, the magnitude of the off-cut leaves little influence on crystal quality, because no obvious differences can be identified among samples with different off-cut angles.

For the comparison of different sample growth conditions, it can be concluded that growth condition of sample BP70 (1250°C, 3 hours) is not optimized since the BP thin film in BP70 has become so thick that microcracking occurs on BP thin film throughout the whole sample surface, indicating that high strain is contained in the thin film.

The crystal quality of the SiC substrate used for BP deposition is predicted to adversely affect

the crystal quality of epitaxial BP thin film. As in BP61, the grazing geometries topograph shows that dislocation density in this sample is higher than others' and also higher strain is contained inside the substrate, meanwhile the transmission topograph reveals that BP thin film is highly distorted in its structure.

Chapter IV. CHARACTERIZATION OF SAPPHIRE SINGLE CRYSTALS

4.1 Edge-defined Film-fed Growth methods

In 1960's, Harold Labelle and Stepanov invented a growth technique used for special shaped crystals including ribbon, tubal and plate crystals, which was named as Edge-defined Film-fed Growth method (EFG)[22,23]. During decades great achievements have been made on growing various shaped single crystal sapphire by EFG method. In this thesis, both the sapphire seed crystals and the sapphire ribbon crystals are grown by this technique.

The schematic diagram of an EFG furnace is presented in Fig. 4-1, where a narrow slit is placed into the alumina melt as the die for crystal growth. Due to the capillary action the melt can rise to the top of the mold, a layer of thin film is formed and then thickened to the surrounding area, while crystallization process occurs from the seed crystal inside. The wetting angle between the mold and the melt should be less than 90° in order to form a fluid film with a certain thickness. The height of the rising melt can be described by:

$$H = 2\gamma \cos\theta / (\rho d g)$$

Where γ is the melt surface tension coefficient (N/cm), θ is the wetting angle, ρ is the melt density (g/cm^3), d stands for the capillary diameter (cm) and g is acceleration of gravity (N/g).

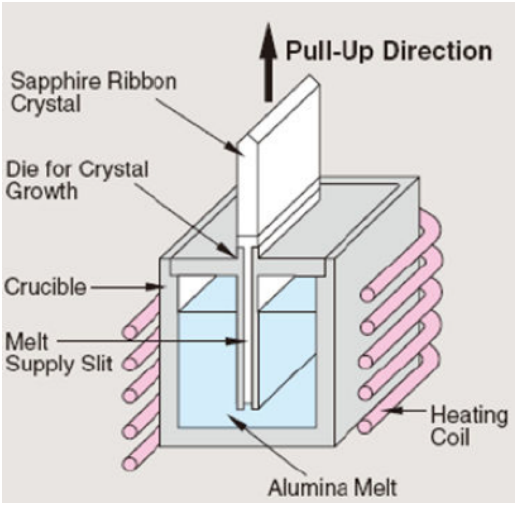

Fig. 4-1 Schematic diagram of an EFG furnace for growing sapphire.

By using EFG method to grow sapphire ribbon crystals, multiple pieces of sapphire can be grown simultaneously; meanwhile the cost is relatively low compared to other

growth methods. The major defects in sapphire grown by EFG method are gas bubbles, inclusions, grain boundaries and heat stress, all of which can be resulted from thermal gradient that mainly exists in the solid-liquid interface.

In order to improve the crystal quality of EFG grown sapphire, synchrotron X-ray topography is carried out to characterize defects generated in both the seed crystal and sapphire ribbon and understand the defect multiplication mechanism.

4.2 Experimental Data Analysis

4.2.1 Characterization of sapphire seed crystals

The seed crystal in EFG method for growing sapphire ribbon is used for initiate the crystallization process by providing a highly ordered crystalline structure in the solid-liquid interface. As a result, the crystal quality of the sapphire ribbon depends greatly on the crystal quality of sapphire seed crystal. Crystal defects that exist near the seed surface, like dislocations, grain boundaries, stacking fault, etc, will degrade the nucleation and crystallization process from the melt to the sapphire ribbon.

In order to obtain information on crystal defects in the sapphire seed, transmission geometry of X-ray topography was carried out to characterize entire region of the seed crystals. The beam size was adjusted to be about 50 mm in width and 4 mm in height. A slit system was deployed to ensure the whole area on the sample to be covered by X-ray beam. Besides, the seed crystal was aligned to the orientation that (0001) basal plane was perpendicular to the incident beam and (1-100) faces horizontally. The schematic diagram of the seed crystal sample A (before growth) and sample B (after growth) are shown below in Fig. 4-2, which have been marked into two parts to analysis separately.

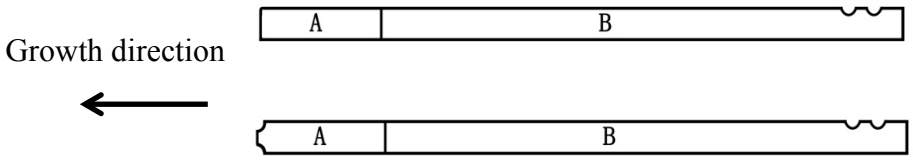

Fig. 4-2 Schematic diagrams of sapphire seed crystals. Above: sample A (before growth). Below: sample B (after growth).

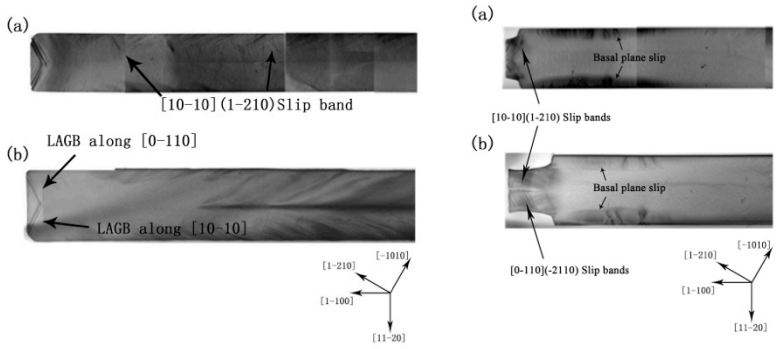

Fig. 4-3 Transmission topographs of part A in sample A (left) and sample B (right).

Fig. 4-3 exhibits transmission topographs of part A (as marked in Fig. 4-2) of two seed crystals. In each figure, the image (b) is taken when the sample in (a) is flipped with regarding to [11-20]. In topographs of sample A, low angle grain boundaries (LAGBs) that form along [10-10] and [0-110] can be observed, resulting in an triangle that sit at the bottom, or the growth front of the seed crystal. The dislocation density is relatively higher near the growth front region. It is possible that these LAGBs are generated by an alignment of basal edge dislocations. Additionally, two sets of slip bands [10-10](1-210) and [0-110](-2110) in the prismatic plane that nucleated from either edge can be observed. The distribution of slip bands is however highly asymmetric. Relatively higher density of basal plane dislocations that arranged in LAGBs is presented in the middle region of sample A. While in topographs of sample B (Fig. 4-3 right), higher density of [0-110](-2110) and [10-10](1-210) slip bands are presented in the growth front region on the left of seed where growth necking phenomenon occurs. Unlike that in sample A, two sets of basal plane slip bands can be obviously observed in the region near the left edge, which are symmetrically distributed along the seed crystal.

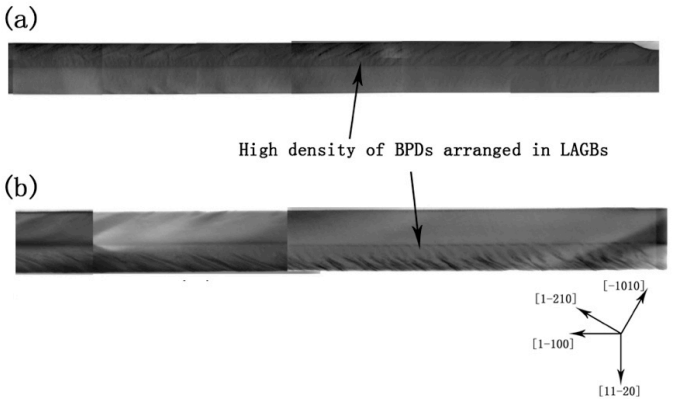

Fig. 4-4 Transmission topographs of part B in sample A.

As for the middle and right region of the seed sample A, transmission topographs in Fig. 4-4 exhibit obvious features of asymmetric distribution of basal plane dislocations. A higher density of dislocation with more well-defined low angle grain boundaries can be observed at the right region on one side of the seed. Fig. 4-5 shows the transmission topographs of sample B. It can be figured out from the topograph that the distribution of dislocations is more symmetric compared with sample A. The overall density of BPD that are arranged in LAGBs is observed to be far less than that in sample A, however, a well-defined low angle grain boundary is observed on one side of the middle-to-right region of the seed crystal. The basal plane dislocation density in that region is much higher than that in the growth front region (Fig. 4-3 right).

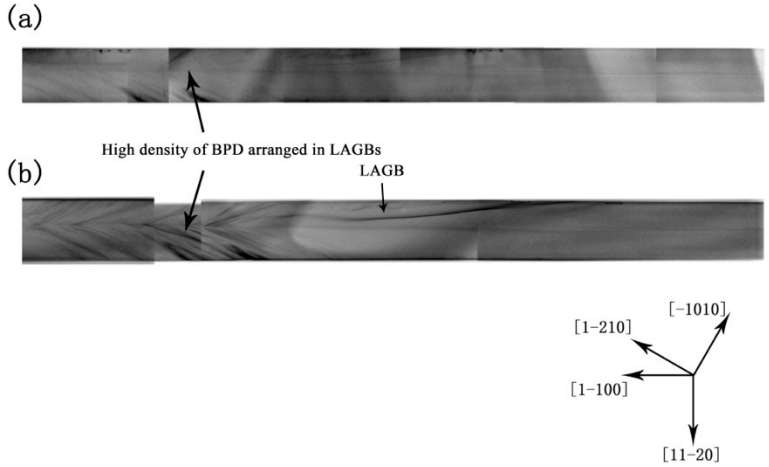

Fig. 4-5 Transimission topographs of part B in sample B.

4.2.2 Characterization of sapphire ribbon crystal

The sapphire ribbon single crystal is much larger in size than the seed. Since the sapphire ribbon is nearly 8 mm thick, which is already too thick for the transmitted X-ray to sustain high enough intensity to form a qualified topograph that could reveal defects in the crystal, reflection geometry was thus carried out. During the experiment session, the whole sapphire ribbon was placed on a sample stage that has motors along X and Y axis so that it can be controlled to move around to ensure that X-ray beam could cover the whole sample. The angle between the (0001) plane normal of the sample and the incident X-ray beam was aligned to be approximately 60° so as to guarantee the high enough intensity of the reflected beam, which could result in an optimized contrast in the topographs. Besides, it can be ensured with a correct incident angle that the reflected spots are separated from overlapping with each other. Fig. 4-6 shows a schematic of the whole sapphire ribbon, with different regions marked into A, B and C for further analysis

separately.

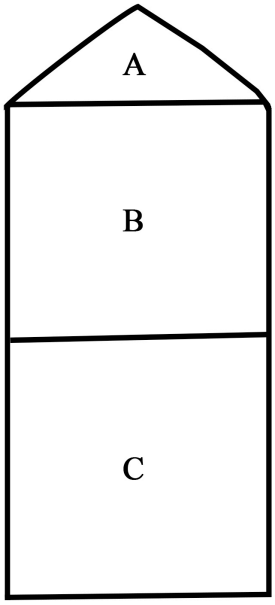

Fig. 4-6 Schematic of sapphire ribbon single crystal, with different regions marked into A, B and C.

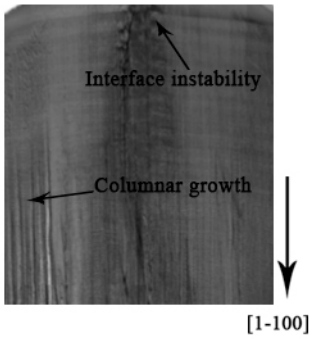

Fig. 4-7 Reflection topograph of sapphire ribbon (part of section A).

Fig. 4-7 and Fig. 4-8 show reflection topographs of corresponding sections in sapphire ribbon crystal. Based on the principles of X-ray topography, only defect information near the sample surface can be obtained through reflection geometry. The surface plane of the ribbon crystal is determined to be (11-20), which coincides with the side plane index of the sapphire seed crystal. As shown in Fig. 4-7, the angular shape at the top is the growth front of the whole ribbon and connects with (1-100) plane of the seed crystal. As the sapphire seed is pulled out from the melt, crystallization occurs at the solid-liquid interface and the shoulder region is then formed due to the capillary effect and the gravity effect on the melt that remains in the crystallization mold. The growth direction of the ribbon is marked [1-100] as in the figure. A series of dislocations that are approximately perpendicular to the growth direction are observed near the top of the ribbon and

continues into the rectangular region of the ribbon. This feature can be a result of instability in the solid-liquid interface, which is likely due to the variation of growth condition in local environment of the crystal.

Additionally, it can be observed clearly from the topograph that there exists a strong evidence for columnar crystal growth mainly located at the upper left region in the ribbon. The upper right region is, however, absent from columnar growth features, thus forming the asymmetric crystal structure during the early stage of crystal growth.

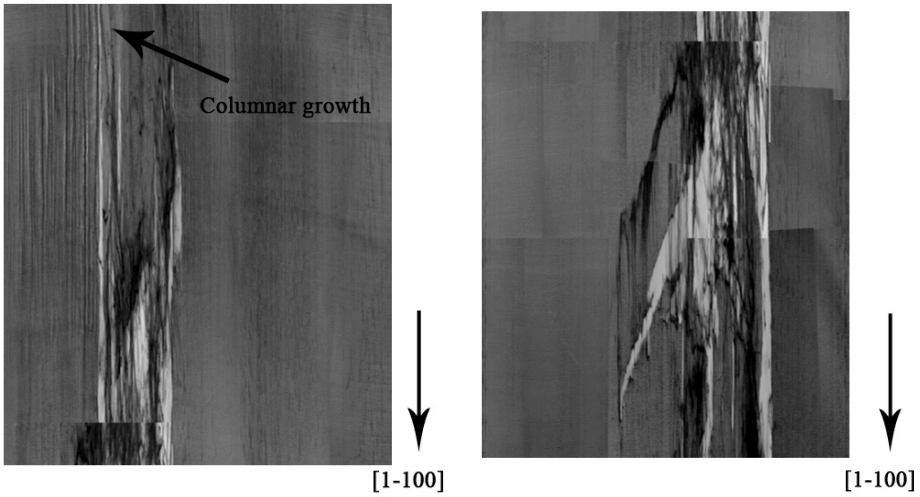

Fig. 4-8 Reflection topograph of sapphire ribbon. Left: part of section B; Right: left part of section C.

The reflection topographs from section B and C in the sapphire ribbon are shown above in Fig. 4-8. The columnar growth that initiate in the upper region continues occur as the sapphire seed is pulled out. The column crystal structure is observed to expand gradually to the left side when the ribbon grows along [1-100] (Fig. 4-8 left), while the initial column structure near the middle of the ribbon grows fast, leading to a polycrystalline structure in the topograph of section C, as shown in Fig 4-8 right that a network of grain boundaries is formed. On the other hand, the right region of the ribbon keeps its single crystalline structure as no further formations of columnar growth are observed throughout the whole ribbon. This could lead to the conclusion that probably due to the instability and inconsistency in growth conditions crystal quality between right side region and left side region is not uniform. Reflection topographs of the right side region exhibits a much better crystal quality than that of the left side region in the sapphire ribbon crystal.

4.3 Discussions and Conclusions

In this chapter, material structure and properties of single crystal sapphire (α-Al_2O_3) and its growth method (Edge-defined Film-fed Growth) were introduced. In order to characterize the crystal quality of sapphire single crystal grown by EFG, an used sapphire seed crystal and a pristine seed crystal were characterized by transmission X-ray topography, while the sapphire ribbon crystal was characterized through reflection geometry.

As for the sapphire seed crystal, transmission topographs show that there exist two sets of slip bands [10-10](1-210) and [0-110](-2110) in the prismatic plane that nucleated from either edge, the distribution of which is symmetric in the used seed crystal and asymmetric in the pristine seed crystal. LAGBs can be observed mainly at the growth front side of the pristine seed crystal, while an obvious well-defined LAGB can be identified at the middle and right region of the used seed crystal. The reason for the asymmetric distribution of dislocations, slip bands and LAGBs can be possibly attributed to the inconsistency in the corresponding growth environment.

For the sapphire ribbon crystal, solid-liquid interface instability is observed near the top of the ribbon and disappears gradually as the crystal grows. Columnar growth occurs at the upper left shoulder region of the ribbon and continues throughout the whole ribbon crystal, with a slight multiplication toward the left edge. This columnar structure finally leads to a polycrystalline structure at the left side, while single crystalline structure sustains itself at the right side. The asymmetric crystal structure probably results from the instable and inconsistent growth condition around the growing environment provided by the EFG furnace.

Chapter V. CONCLUSIONS

i. Crystal quality of boron phosphide thin film deposited on different SiC substrates by Chemical Vapor Deposition is characterized using synchrotron X-ray topography and other techniques including optical microscopy and scanning electron microscopy.

(1) Based on transmission topography results, the stacking relation between BP epitaxial thin film and SiC substrate is determined to be (0001)/[11-20]-SiC // (111)/[1-10]-BP, in which a mismatch of about 4% is presented.

(2) The overall crystal quality of samples with 4H-SiC substrates is comprehensively better than samples with 6H-SiC substrates, as concluded from transmission topographs of 4H-SiC samples where diffracted spots from (111)-$B_{12}P_2$ and twinned (111)-$B_{12}P_2$ are absent. Besides, sample BP45 with 4H-SiC as the substrate exhibits the best quality since it possesses the least amount of twinned (111)-BP and the lowest strain in BP thin film from the transmission topograph.

(3) Samples that contain an off-cut angle between their (0001) basal plane and sample surface has nearly identical crystal quality in comparison with the on-axis sample, based on the evidence that these two types of samples exhibit undistinguishable intensity difference between twinned (111)-BP and (111)-$B_{12}P_2$ and also exhibit the same amount of distortion of these diffracted spots. In addition, the magnitude of the off-cut leaves little influence on crystal quality, because no obvious differences can be identified among samples with different off-cut angles.

(4) For the comparison of different sample growth conditions, it can be concluded that growth condition of 1250°C and 3 hours is not optimized since the BP thin film deposited under such condition has become so thick that microcracking occurs on BP thin film throughout the whole sample surface, indicating that high strain is contained in the thin film.

(5) The crystal quality of the SiC substrate untwinned for BP deposition is predicted to adversely affect the crystal quality of epitaxial BP thin film. As in BP61, the grazing geometries topograph shows that dislocation density in this sample is higher than others' and also higher strain is contained inside the substrate, meanwhile the transmission topograph reveals that BP thin film is highly distorted in its structure.

ii. Crystal quality and defect structures of single crystal sapphire seed and ribbon grown by Edge-defined Film-fed Growth method are studied by synchrotron X-ray topography,

using the reflection geometry.

(1) As for the sapphire seed crystal, transmission topographs show that there exist two sets of slip bands [10-10](1-210) and [0-110](-2110) in the prismatic plane that nucleated from either edge, the distribution of which is symmetric in the used seed crystal and asymmetric in the pristine seed crystal. LAGBs can be observed mainly at the growth front side of the pristine seed crystal, while an obvious well-defined LAGB can be identified at the middle and right region of the used seed crystal.

(2) For the sapphire ribbon crystal, solid-liquid interface instability is observed near the top of the ribbon and disappears gradually as the crystal grows. Columnar growth occurs at the upper left shoulder region of the ribbon finally leads to a polycrystalline structure at the left side, while single crystalline structure sustains itself at the right side. The asymmetric crystal structure probably results from the instable and inconsistent growth condition around the growing environment provided by the EFG furnace.

Chapter VI. FUTURE WORK

Based on the study on the transmission X-ray topographs of BP thin film deposited on SiC substrates, differences between relative intensities of the BP diffraction pattern and simulated BP pattern remain to be understood. The actual structure of cubic BP might be obtained by editing atom positions in LauePt program to make the simulated pattern match with the diffraction pattern. Other characterization technique, such as high-resolution transmission electron microscopy (HRTEM) can be carried out to study the thin film structure especially the structure at the epilayer-substrate interface. Additionally, multiple samples with a larger variety of growth conditions need to be characterized in order to obtain systematic information on the influence of growth conditions on crystal quality.

As for sapphire single crystal grown by EFG, formation mechanisms of LAGBs in the seed crystal and columnar growth phenomenon in the sapphire ribbon remain to be understood by further defect characterization on different slices from different area of the sapphire ribbon.

REFERENCES

1. Crane, T. W.; Baker, M. P. Neutron Detectors; pp. 379–406.
2. Shigemi Yugo, Takashi Sato, and Tadamasa Kimura, Thermoelectric figure of merit of boron phosphide, Applied Physics Letters **46**, 842 (1985).
3. R. J. Archer, R. Y. Koyama, E. E. Loebner, and R. C. Lucas, Phys. Rev. Lett. 12, 538 (1964).
4. R. A. Burmeister and P. E. Greene, Bull. Amer. Phys. Soc. 10, 1184 (1965).
5. F. V. Williams and R. A. Ruehrwein, J. Amer. Chern. Soc. 82,1330 (1960).
6. H. Morkoç, S. Strite, et al, Large-band-gap SiC, III-V nitride, and II-VI ZnSe-based semiconductor device technologies, Journal of Applied Physics 76, 1363 (1994).
7. J. J. Sumakeris, J. R. Jenny, and A. R. Powell, MRS Bulletin 2005, 30, 280.
8. H. Matsunami, Jpn. J. Appl. Phys. 2004, 43, 6835.
9. T.L. Chu, J.M. Jackson, A.E. Hyslop, and S.C. Chu, J Appl Phys 42, 420 (1971).
10. Dongsheng Peng, Ke Jin, Fa Dong, Jianhua Wei, The Study of Pretreated Sapphire Substrate, 978-1-4244-6554-5/11 2011 IEEE.
11. Huili Tang, Hongjun Li and Jun Xu, Growth and Development of Sapphire Crystal for LED Applications, Advanced Topics on Crystal Growth, pp. 310-312.
12. Hosseini S M, Aliabad H A R, Kompany A.. First-principles Study of the Optical Properties of Pure α-Al2O3 and La aluminates. Eur Phys J B 2005; 43(4): 439-444.
13. B.D. Cullity, Elements of X-ray Diffraction. (1956).
14. M.V. Laue, Ann Phys., 26: pp. 55-68 (1936).
15. David R. Black, Gabrielle G. Long, X-ray Topography, Special Publication 960-10.
16. Herman Winick, S. Doniach, Synchrotron Radiation Research. Plenum Press. (1980).
17. D. K. Bowen and B. K. Tanner, in "*High Resolution X-Ray Diffractometry and Topography*", Taylor & Francis, pp. 225 (1998).
18. Raghothamachar, B., et al., Defect analysis in crystals using X-ray topography. Microscopy Research and Technique, 2006. 69(5): p. 343-358.
19. J. Goldstein, D. Newbury, et al. Scanning Electron Microscopy and X-ray Microanalysis, 2003 Kluwer Academic/Plenum Publishers, Third edition.
20. Chu, T. L.; Jackson, J. M.; Hyslop, A. E.; Chu, S. C. Crystals and epitaxial layers of boron phosphide. Journal of Applied Physics 1971, 42, 420.
21. Shohno, K.; Takigawa, M.; Nakada, T. Epitaxial growth of BP compounds on Si substrates using the B2H6-PH3-H2 system. Journal of Crystal Growth 1974, 24-25, 193– 196.

22. BunoiuOM, NicoaraI, SantaillerJL, et al. On the void distribution and size in shaped sapphire crystals. Cryst Res Technol, 2005;40(9) 852-859.
23. H.E. LaBelle, J. Crystal Growth 50 (1980) 8.